Journal of Magnetic Resonance 203 (2010) 257–273

Contents lists available at ScienceDirect

Journal of Magnetic Resonance

journal homepage: www.elsevier.com/locate/jmr

Mechanism of ^{1}H–^{14}N cross-relaxation in immobilized proteins

Erik P. Sunde, Bertil Halle *

Biophysical Chemistry, Center for Molecular Protein Science, Lund University, SE-22100 Lund, Sweden

ARTICLE INFO

Article history:
Received 6 November 2009
Available online 25 January 2010

Keywords:
Quadrupolar dip
Polarization transfer
Internal water
Hydrogen exchange
Water relaxation

ABSTRACT

A resonant enhancement of the water-^{1}H relaxation rate at three distinct frequencies in the range 0.5–3 MHz has been observed in a variety of aqueous biological systems. These so-called quadrupole (Q) peaks have been linked to a dipolar flip–flop polarization transfer from ^{1}H nuclei to rapidly relaxing amide ^{14}N nuclei in rotationally immobilized proteins. While the Q-peak frequencies conform to the known amide ^{14}N quadrupole coupling parameters, a molecular model that accounts for the intensity and shape of the Q peaks has not been available. Here, we present such a model and test it against an extensive set of Q-peak data from two fully hydrated crosslinked proteins under conditions of variable temperature, pH and H/D isotope composition. We propose that polarization transfer from bulk water to amide ^{14}N occurs in three steps: from bulk water to a so-called intermediary proton via material diffusion/exchange, from intermediary to amide proton by cross-relaxation driven by exchange-mediated orientational randomization of their mutual dipole coupling, and from amide proton to ^{14}N by resonant dipolar relaxation 'of the second kind', driven by ^{14}N spin fluctuations, which, in turn, are induced by restricted rigid-body motions of the protein. An essentially equivalent description of the last step can be formulated in terms of coherent $^{1}H \rightarrow {}^{14}N$ polarization transfer followed by fast ^{14}N relaxation. Using independent structural and kinetic information, we show that the Q peaks from these two proteins involve $\sim$7 intermediary protons in internal water molecules and side-chain hydroxyl groups with residence times of order 10^{-5} s. The model not only accounts quantitatively for the extensive data set, but also explains why Q peaks are hardly observed from gelatin gels.

1. Introduction

When a spin $I = 1/2$ nucleus is dipole-coupled to a rapidly relaxing spin $S \geq 1$ nucleus with a static residual quadrupole coupling, enhanced I-spin relaxation is observed at I-spin Larmor frequencies matching an eigenfrequency of the static S-spin Hamiltonian. This resonant cross-relaxation phenomenon has been widely exploited for structural and dynamic studies of solids and liquid crystals [1–8]. When observed against the background of the field-dependent longitudinal I-spin relaxation, the resonant enhancement of the I-spin relaxation induced by the S spin is commonly referred to as a quadrupole peak (Q peak, QP) in the relaxation rate or as a quadrupole dip in the relaxation time.

For biological systems, Q peaks were first observed in protein powders and attributed to ^{1}H–^{14}N spin pairs [9], which were also thought to be of critical importance for the background ^{1}H relaxation dispersion from aqueous biological systems, including tissues [10–12]. The latter idea was refuted by the observation that $^{14}N \rightarrow {}^{15}N$ substitution removes the Q peaks but has little effect on the background dispersion [13]. Subsequently, ^{1}H–^{14}N Q peaks from a wide range of biological systems have been reported by several groups [13–19]. Under resonant conditions, the ^{14}N spins can evidently act as a relaxation sink not only for protein protons but also for the water-^{1}H magnetization, even in systems with high water content, as long as the protein component is immobilized on the time scale of the inverse static ^{14}N quadrupole coupling. Current interest in 'biological' Q peaks is fuelled by potential applications in cell biology, e.g. for monitoring protein immobilization *in vivo* [18,19], and by the quest for new contrast modalities in clinical MRI [20]. To realize the full potential of the QP phenomenon in these areas, a thorough understanding of the underlying mechanism is needed.

Although the QP phenomenon has been analyzed theoretically from different perspectives [3,7,9,13,15,21–23], the detailed molecular mechanism of the ubiquitous ^{1}H–^{14}N Q peaks in biological systems has not been established. The positions of the Q peaks can be accurately predicted from the principal components of the ^{14}N residual quadrupole tensor, but a rigorous theory that can also predict the intensities (absolute and relative) and the width and shape of the Q peaks has not been available. By $^{14}N \rightarrow {}^{15}N$ substitution, Kimmich and coworkers convincingly demonstrated that ^{14}N spins are responsible for the Q peaks [13]. Furthermore, a comparison of Q-peak frequencies with ^{14}N quadrupole coupling constants from

* Corresponding author. Fax: +46 46 222 4116.
E-mail address: bertil.halle@bpc.lu.se (B. Halle).

1090-7807/$ - see front matter © 2010 Elsevier Inc. All rights reserved.
doi:10.1016/j.jmr.2010.01.008

NQR [24] or MAS NMR [25] studies of crystalline materials unambiguously identified the relaxation sinks as amide rather than amino nitrogens [11]. It is also clear that polarization transfer from ^{1}H to ^{14}N involves dipolar flip–flop transitions under level-matching conditions. However, several key aspects of the mechanism remain obscure. (1) How many steps are required to transfer water-^{1}H polarization to ^{14}N? (2) Which protons act as intermediates along this pathway? (3) By what mechanism is magnetization relayed between protons in the different steps of the pathway: dipolar cross-relaxation, spin diffusion or material exchange? (4) If ^{1}H–^{1}H cross-relaxation is involved, what motion modulates the dipole coupling? (5) How should the final ^{1}H → ^{14}N polarization step be described, as a coherent process [3] or as a motionally induced cross-relaxation [9]? (6) In the latter case, what is the motion? Several tentative answers have been given to most of these questions, but a complete model has not been presented that quantitatively accounts for the Q peaks in any biological system.

To elucidate the mechanism of ^{1}H–^{14}N Q peaks in aqueous biological systems, we use as model systems the proteins bovine pancreatic trypsin inhibitor (BPTI) and mammalian ubiquitin (mUb), chemically crosslinked by glutaraldehyde [26,27] at a protein concentration of ∼10% (3000–4000 water molecules per protein molecule). These proteins have been extensively characterized with respect to structure [28,29], labile-hydrogen exchange [30–34], internal water exchange [35–37] and external hydration dynamics [38]. We present an extensive set of QP data from these model systems, including variable temperature and pH, and H → D substitution in the protein or water component. We also present QP data from a gelatin gel.

After extracting the Q peaks from the low-frequency water-^{1}H magnetic relaxation dispersion (MRD) profile measured with the field-cycling technique (Sections 2 and 3), we analyze the QP data in a model-independent way in Section 4. Guided by the results of this analysis, we then develop a detailed model and show that it accounts quantitatively for the observations (Section 4). A key role in the model is played by so-called intermediary protons in internal water molecules and/or hydroxyl groups, the exchange of which is responsible for the first two steps in the magnetization transfer pathway: material exchange from bulk water to intermediary proton and dipolar cross-relaxation between the intermediary and amide protons, driven by exchange-mediated orientational randomization (EMOR) of the dipole coupling. The last step of the mechanism is dipolar relaxation 'of the second kind' of the amide proton, driven by ^{14}N spin fluctuations in a process that is closely analogous to paramagnetic ^{1}H relaxation enhancement by a static zero-field splitting in the low-field and slow-tumbling limits [22,39–45]. In Appendix A, we demonstrate that the alternative view of this step as a coherent ^{1}H → ^{14}N polarization transfer [3,5] followed by fast ^{14}N relaxation is essentially equivalent to the former picture of dipolar ^{1}H relaxation driven by ^{14}N spin fluctuations.

2. Materials and methods

2.1. Sample preparation

Bovine pancreatic trypsin inhibitor (BPTI, trade name Trasylol®, batch 9104, 97% purity by HPLC) was obtained from Bayer HealthCare AG (Wuppertal, Germany). To remove residual salt, the protein was exhaustively dialyzed against Millipore water (Millipore, Billerica, MA) and lyophilized. Mammalian ubiquitin (mUb) was expressed in *Escherichia coli* and purified to >99% as described [37]. Deuterated mUb (*d*-mUb) was expressed in a D_2O-based minimal medium with glucose as the only carbon source and purified in the same way as unlabeled mUb. Analysis of ^{1}H spectra showed that 83% of the non-exchangeable protein protons were substituted by deuterons [46]. Lyophilized protein was dissolved in ultrapure H_2O (Fluka Biochimika), in 75 mM PIPES (piperazine-*N*-*N*′-bis[2-ethane-sulfonic acid]) buffer (Sigma–Aldrich, St. Louis, MO) in H_2O, or in mixtures of H_2O and 99.9% D_2O (Spectra Stable Isotopes, Columbia, MD). Prior to NMR experiments on mixed-solvent samples, 10–12 days were allowed for H → D exchange with the protein. Solution pH was adjusted by μl additions of HCl or NaOH, followed by centrifugation. The protein concentration was determined before crosslinking by complete amino acid analysis (performed at the Amino Acid Analysis Center, Dept. of Biochemistry and Organic Chemistry, Uppsala University, Sweden) or by absorbance at 280 nm. The protein was crosslinked by addition of ice-cold 25% glutaraldehyde (GA) solution (MP Biomedicals Inc., Solon, OH) as described [37]. Table 1 shows the composition of all samples examined by ^{1}H MRD.

The bifunctional crosslinking reagent GA has been widely used for protein immobilization [26]. GA reacts primarily with lysine (and N-terminal) amino groups [27], forming stable crosslinks by a mechanism that has not been firmly established [26]. The GA/lysine stoichiometry of the reaction is reported [47] to be ∼4 and N_{GA} was chosen to allow essentially all amino groups in BPTI (5) and ubiquitin (8) to participate in crosslinks. The amino groups are fairly uniformly distributed over the protein surfaces.

Gelatin type B from bovine skin was used as supplied by Sigma (product no. G9382). The amino acid composition of this preparation has been reported [48] and the average molecular weight is ∼50 kDa, corresponding to ∼550 residues. The physical gel was prepared by cooling from 60 °C as described [48].

2.2. Relaxation measurements

The water-^{1}H longitudinal relaxation rate, R_1, was measured from 5 kHz to 600 MHz using seven different NMR spectrometers [37]. A dense frequency sampling was used in the range, 1.5–3.6 MHz, of the Q_- and Q_+ peaks and, in some cases, in the range, 0.4–1.5 MHz, of the Q_0 peak. The R_1 data in the QP range were measured on a 1 T Stelar fast-field-cycling instrument with polarization at 40 MHz and detection at 16.6 MHz, a field switching time of 3 ms, and a 90° pulse length of 6.1 μs. The polarization and recovery times were set to 4 T_1 and the number of accumulated transients was 8 for all samples except B4, where either 4 (B4a–c) or 20 (B4d) transients were used. The sample temperature was maintained at 20.0 ± 0.1 °C, except for sample B3 where it was varied from 5.0 to 60.0 °C.

2.3. Data treatment

The measured longitudinal relaxation rate, R_1, of the bulk-water-^{1}H resonance consists of a background contribution, R_1^0,

Table 1
Sample composition.

Label	Protein	pH	T (°C)	X_H[a]	N_W[b]	N_{GA}[c]
B1	BPTI	4.2	20	1	3058	22
B2	BPTI	5.1[d]	20	1	2956	21
B3	BPTI	4.3	5–60	1	4193	34
B4a	BPTI	4.2	20	1	3253	26
B4b	BPTI	4.3	20	0.550	3506	28
B4c	BPTI	4.3	20	0.267	3616	29
B4d	BPTI	4.3	20	0.199	3921	30
U1	mUb	5.3[d]	20	1	3795	27
U2	*d*-mUb	5.3[d]	20	1	4286	31

[a] Atom fraction H in solvent.
[b] Water/protein mole ratio.
[c] GA/protein mole ratio.
[d] Buffer present.

and a QP contribution, R_1^Q, due to polarization transfer to amide ^{14}N nuclei in the protein,

$$R_1(\omega_0) = R_1^0(\omega_0) + R_1^Q(\omega_0) \quad (1)$$

The QP contribution was obtained by subtracting the background contribution from the measured R_1 at each frequency. The function $R_1^0(\omega_0)$ was constructed from a multi-Lorentzian fit to R_1 data in the frequency range 0.1–50 MHz, excluding the narrow intervals of the Q peaks (Fig. 1a). All QP relaxation rates were scaled to the same water/protein mole ratio, $N_W = 3000$, using the proportionality $R_1^Q \propto 1/N_W$ (Section 5.1).

To characterize the Q peaks, the R_1^Q data were fitted to a sum of 2 or 3 Gaussians (Fig. 1b)

$$R_1^Q(\nu_0) = \sum_\alpha C_\alpha (2\pi\sigma_\alpha^2)^{-1/2} \exp\left[-\frac{1}{2}\left(\frac{\nu_0 - \nu_\alpha}{\sigma_\alpha}\right)^2\right] \quad (2)$$

the Q peaks being labeled with $\alpha = 0$, − and + in order of increasing frequency (Fig. 1). Each Q peak was thus characterized by three parameters: (1) the peak frequency ν_α, (2) the FWHM peak width, $\Delta_\alpha = 2\ \sigma_\alpha\ (2\ \ln 2)^{1/2}$, and (3) either the integrated peak intensity C_α or the peak amplitude $C_\alpha(2\pi\sigma_\alpha^2)^{-1/2}$. In most cases, the frequency sampling was not sufficiently dense to fit the small Q_0 peak. Lorentzians fits to the Q peaks were less satisfactory (Fig. 1c). All fits were performed with Marquardt–Levenberg least-squares minimization [49]. The powder averages required to fit the model to the R_1^Q data were computed numerically with the ZCW scheme [50].

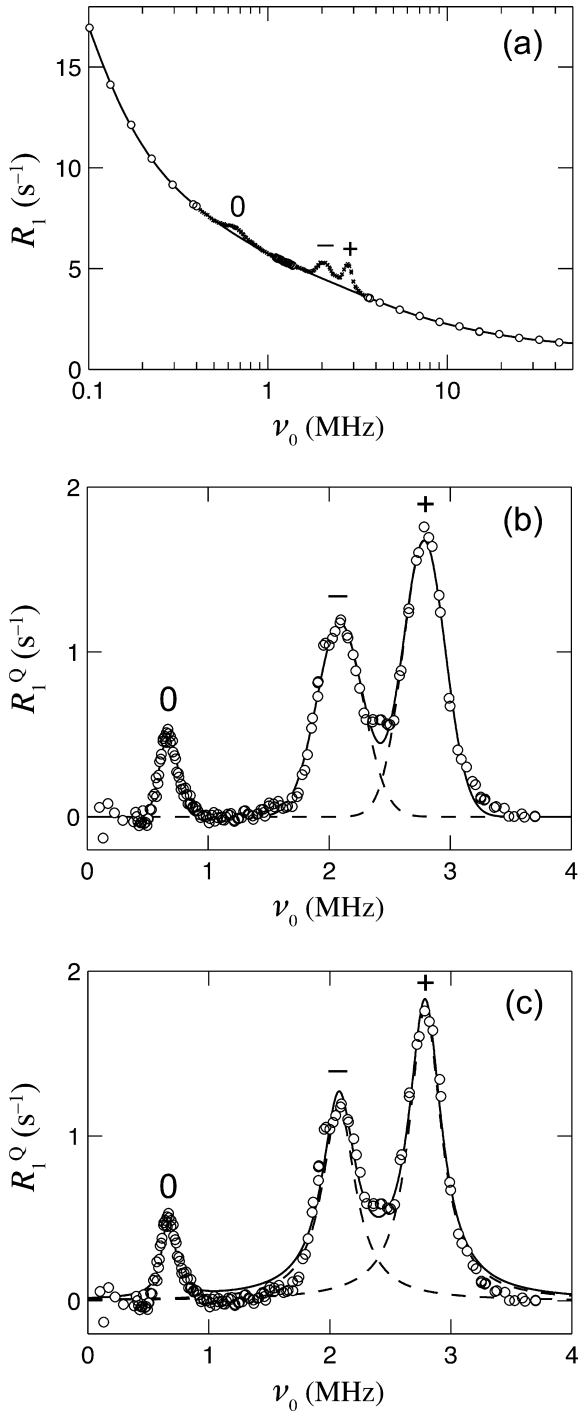

Fig. 1. R_1 data for BPTI, sample B3 at 10 °C. (a) Multi-Lorentzian fit to background dispersion (○), excluding data in the QP ranges (×). (b) Gaussian and (c) Lorentzian fits to the Q peaks.

3. Observations

The QP relaxation rate, $R_1^Q(\omega_0)$, was determined by subtracting the monotonic background relaxation dispersion from the measured R_1 (Section 2.3). The Q peaks were characterized in terms of peak frequency (ν_α), integrated peak intensity (C_α) and FWHM peak width (Δ_α), determined from Gaussian fits (Section 2.3). QP data were obtained for two crosslinked proteins, BPTI and mUb, under variable conditions of temperature, pH and H/D isotope composition of the protein and solvent (Table 1).

3.1. Temperature dependence

The temperature dependence of the Q peaks was examined for BPTI from 5 to 60 °C. Over this range, the Q_- and Q_+ peak frequencies decrease linearly by 2.5% (Fig. 2a). The Q_0 peak was only sampled sufficiently densely to allow a Gaussian fit at three temperatures (10, 20 and 45 °C). At these temperatures, ν_0 conforms to within 5% with the theoretical expectation that $\nu_0 = \nu_+ - \nu_-$ (Section 4.1). The linewidths do not show a significant temperature dependence (Fig. 2c). The Q_- and Q_+ peaks have similar widths, while Q_0 is more narrow: $\Delta_0 = 0.18 \pm 0.02$, $\Delta_- = 0.47 \pm 0.02$ and $\Delta_+ = 0.42 \pm 0.01$ MHz in the 10–45 °C range. The integrated peak intensity varies nonmonotonically, with a weak minimum near 20 °C and a weak maximum near 50 °C (Fig. 2b). The Q_- and Q_+ intensities have the same temperature dependence. Averaged over the range 10–45 °C, the peak intensities are $C_0 = 0.10$, $C_- = 0.65$ and $C_+ = 0.82$ MHz s^{-1}.

3.2. pH dependence

The pH dependence of the Q peaks was examined for BPTI (Fig. 3 and Table 2). Upon increasing pH from 4.2 to 5.1, we observe a slight (20–30 kHz) upshift of the peaks and a more significant ~20% reduction of the integrated intensity of the two peaks.

3.3. Solvent H → D substitution

The effect on the Q peaks of partial H → D substitution in the water solvent and the labile hydrogens in the protein was examined by studying BPTI in H_2O/D_2O solvent mixtures with the proton fraction, X_H, varying from 0.20 to 1.00. H → D substitution has no significant effect on the peak frequencies (Fig. 4a), $\nu_- = 2.069 \pm 0.006$ and $\nu_+ = 2.764 \pm 0.004$ MHz, or on the linewidths (Fig. 4c), $\Delta_- = 0.46 \pm 0.02$ and $\Delta_+ = 0.40 \pm 0.03$ MHz. In contrast, the Q-peak intensities are gradually reduced towards zero as protons are replaced by deuterons (Fig. 4b), consistent with previous re-

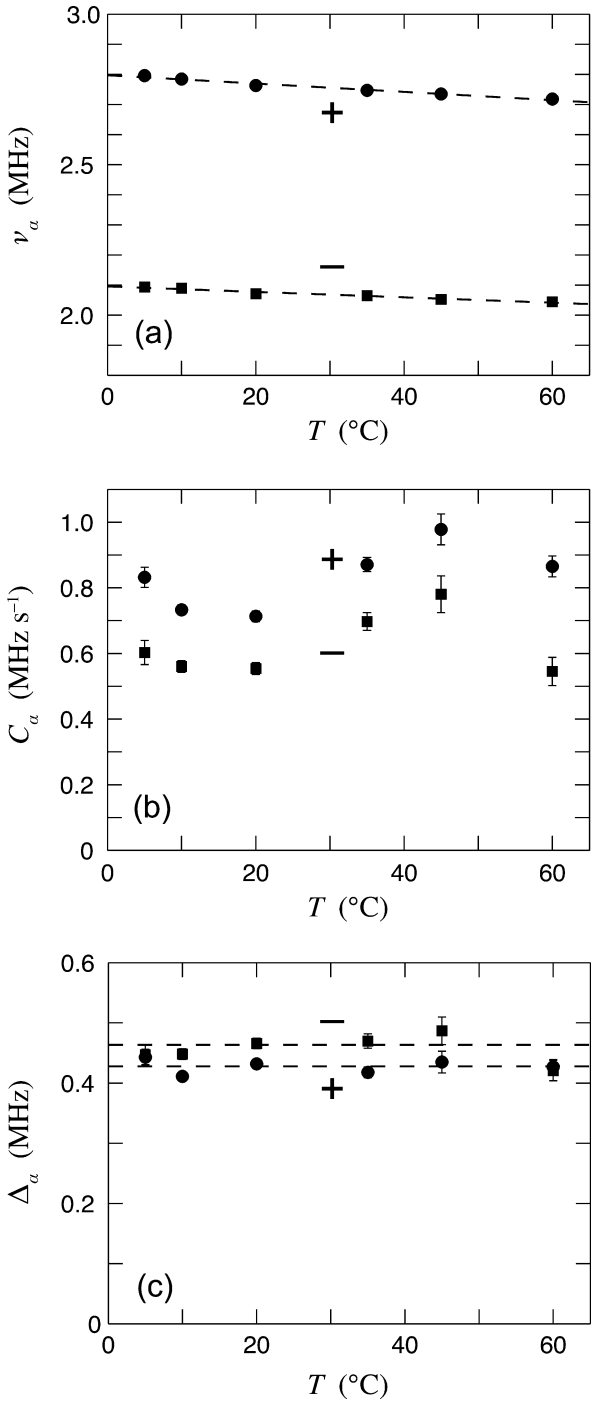

Fig. 2. Temperature dependence of (a) frequency, (b) integrated intensity, and (c) FWHM width of the Q_- and Q_+ peaks from BPTI sample B3.

ports of reduced Q-peak intensity on $H_2O \rightarrow D_2O$ substitution at lower water content [13,14,17].

3.4. BPTI versus mUb

Fig. 5 compares the Q peaks from BPTI (sample B2) and mUb (sample U1) at similar pH values. As in the other figures, these R_1^Q data have been normalized to the same water/protein mole ratio, $N_W = 3000$, but mUb is a larger protein than BPTI (8.6 versus 6.5 kDa) and has 40% more protonated amide nitrogens (80 versus 57). Despite these differences, the Q peaks from the two proteins

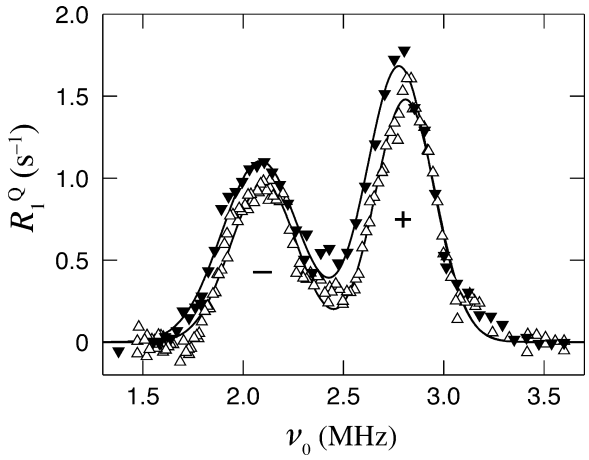

Fig. 3. Q_- and Q_+ peaks from BPTI at pH 4.2 (sample B1, ▼) and pH 5.1 (sample B2, △) with Gaussian fits (curves).

Table 2
Parameter values from Gaussian fits to the Q_- and Q_+ peaks.

Parameter	BPTI pH 4.2	BPTI pH 5.1	mUb	*d*-mUb
ν_- (MHz)	2.087(6)	2.103(4)	2.095(4)	2.104(4)
C_- (MHz s^{-1})	0.53(3)	0.41(2)	0.40(2)	0.43(2)
Δ_- (MHz)	0.45(1)	0.40(1)	0.38(1)	0.43(1)
ν_+ (MHz)	2.777(4)	2.809(3)	2.786(2)	2.780(3)
C_+ (MHz s^{-1})	0.68(2)	0.56(1)	0.59(1)	0.55(1)
Δ_+ (MHz)	0.38(1)	0.36(1)	0.36(1)	0.40(1)

Uncertainty in last digit (one standard deviation) given within parentheses.

are nearly superimposed and the small differences in the Gaussian parameters are hardly significant (Table 2).

3.5. Protein H → D substitution

We also examined a partially deuterated form of mUb, with 83% of the nonlabile protons replaced by deuterons [46], while all the labile hydrogens, including the amide hydrogens, carry protons. The Q peaks of *d*-mUb differ very little from those of mUb, the only significant difference being a slight suppression of the Q_+ peak (Fig. 6).

4. Model-independent analysis

4.1. Q-peak frequencies

There is general agreement that the three Q peaks correspond to transitions between the three nondegenerate eigenstates of the static ^{14}N spin Hamiltonian. Indeed, Kimmich et al. showed that the Q peaks observed from green algae disappear when the proteins are extensively ^{15}N-labeled [13]. Q peaks are not seen for isotropically tumbling proteins, but require immobilization on the time scale of the inverse quadrupole coupling (~50 ns), leading to a static residual quadrupole coupling $\bar{\omega}_Q$. At the MHz ^{1}H frequencies where the Q peaks occur, the ^{14}N Larmor frequency is only 50–200 kHz so the static ^{14}N spin Hamiltonian is dominated by the residual quadrupole coupling. To first order in the small Zeeman coupling, the three ^{14}N transition frequencies are [9]

$$\Omega_\pm = \frac{3}{4}\bar{\omega}_Q \pm \Delta \tag{3a}$$

$$\Omega_0 = 2\Delta \tag{3b}$$

where

$$\bar{\omega}_Q = S_G \omega_Q \tag{4}$$

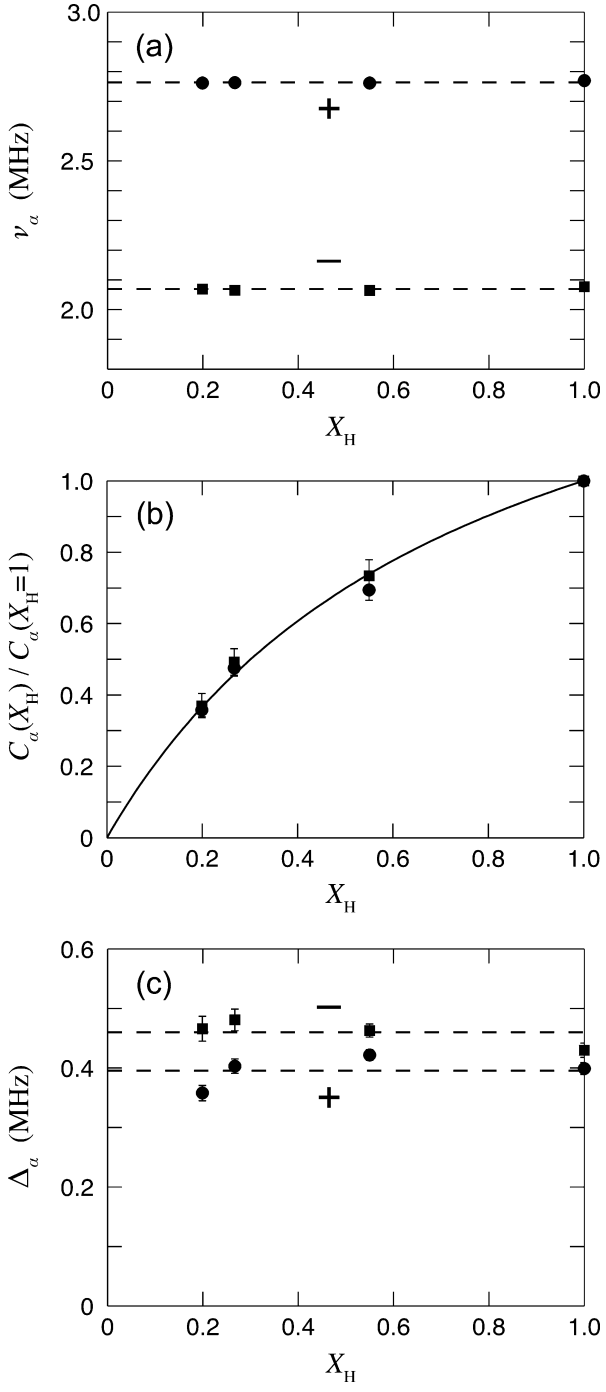

Fig. 4. Dependence on solvent proton fraction, X_H, of (a) frequency, (b) integrated intensity (normalized to $X_H = 1$), and (c) FWHM width of the Q$_-$ and Q$_+$ peaks from BPTI samples B4a–d. The significance of the fitted curve in (b) is explained in Section 4.2.

$$\Delta = \left[\left(\frac{\eta\bar{\omega}_Q}{4}\right)^2 + (\omega_{0,N}\cos\beta_{LF})^2\right]^{1/2} \quad (5)$$

Here, ω_Q is the ^{14}N quadrupole coupling constant, η is the asymmetry parameter of the ^{14}N electric field gradient (EFG) tensor, and β_{LF} is the angle between the axis of the major principal EFG component and the $\boldsymbol{B}_0$ field. Further, $\omega_{0,N} = \omega_0(^{14}N)$ and S_G is an orientational order parameter describing the effect of partial motional averaging of the EFG by motions on time scales shorter than ~50 ns (see below).

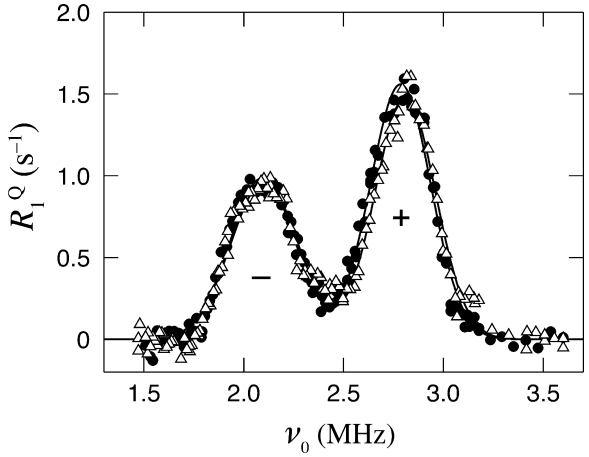

Fig. 5. Q$_-$ and Q$_+$ peaks from BPTI sample B2 (△) and from mUb sample U1 (●) with Gaussian fits (curves).

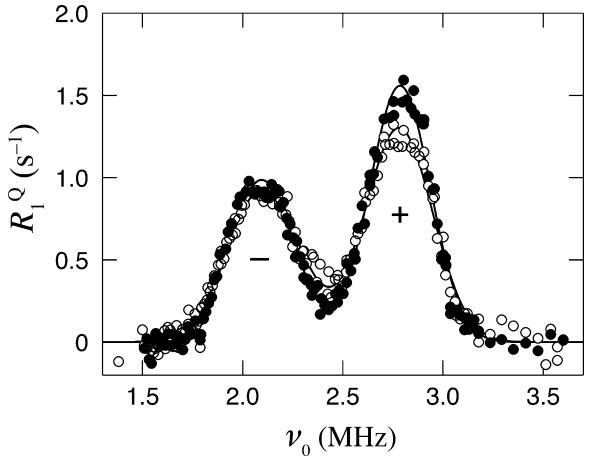

Fig. 6. Q$_-$ and Q$_+$ peaks from mUb (sample U1, ●) and *d*-mUb (sample U2, ○) with Gaussian fits (curves).

If we identify the peak frequencies ν_α with the transition frequencies Ω_α, then the observed values $\nu_- \approx 2.1$ MHz and $\nu_+ \approx 2.8$ MHz (Table 2 and Fig. 2) yield with Eq. (3a) $\bar{\nu}_Q \approx 3.3$ MHz. Using Eq. (5) with the second term neglected, we also obtain $\eta \approx 0.4$. These ^{14}N quadrupole parameters are consistent with the values, $\bar{\nu}_Q = 3.0$–3.5 MHz and $\eta = 0.37$–0.42, obtained from NQR studies of H-bonded amide nitrogens in oligo-glycine crystals at 77 K [24]. In contrast, $\bar{\nu}_Q$ is only 1.1–1.3 MHz for the α-ammonium group in amino acids [25], which would yield Q$_\pm$ peaks below 1 MHz. Presumably, the ammonium and guanidinium groups of lysine and arginine side-chains have a similarly small quadrupole coupling. As previously concluded [11], the observed Q peaks can be linked to ^{14}N nuclei in backbone peptide groups and, possibly, to amide groups in asparagine and glutamine side-chains. Conversely, a viable QP model must explain why ^{14}N in ammonium and guanidinium groups do not produce Q peaks.

We attribute the weak linear decrease of the Q$_\pm$ peak frequencies with increasing temperature (Fig. 2a) to thermal motional averaging of the quadrupole coupling. Assuming isotropic (but restricted) motional averaging, so that η is constant, the observed temperature dependence in the frequencies $\nu_\pm$ can be linked to the global order parameter S_G. Indeed, for classical small-amplitude harmonic fluctuations, we expect that

$$S_G(T) = 1 - \frac{3}{2}\langle\theta^2\rangle = 1 - aT \quad (6)$$

The linear fits shown in Fig. 2a yield $a = 3.9 \times 10^{-4}$ and $4.4 \times 10^{-4}\,K^{-1}$ for the two peaks. At 20 °C, this corresponds to $S_G = 0.88$ and a RMS angular fluctuation of 16 degrees.

The motion responsible for partial averaging of the quadrupole coupling may occur on any time scale up to ~50 ns. A plausible candidate is the 'rocking' motion of the flexibly crosslinked protein, which is expected to occur on the nanosecond time scale of free-protein tumbling. Such restricted rigid-body rotation is a powerful relaxation mechanism for the ^{14}N spin. Since both the ^{14}N Larmor frequency, $\nu_{0,N}$ (<100 kHz), and the ^{14}N quadrupole frequency, $\bar{\nu}_Q$ (~3.3 MHz), are small compared to the inverse correlation time, relaxation is in the extreme motional-narrowing limit. Ignoring an orientation-dependent factor of order unity, the quadrupolar relaxation rate is then given by [1,37]

$$R_Q = \frac{3}{8}\left(1 - S_G^2\right)\omega_Q^2\tau_Q = \frac{3}{8}\left(S_G^{-2} - 1\right)\bar{\omega}_Q^2\tau_Q \tag{7}$$

With $\bar{\nu}_Q$ = 3.3 MHz, $S_G = 0.88$ and, say, $\tau_Q = 7$ ns, Eq. (7) predicts a quadrupolar relaxation time, $1/R_Q = 3$ μs. This order-of-magnitude estimate is consistent with the general view that the Q peaks are caused by ^{14}N nuclei acting as relaxation sinks for the water-^1H magnetization. Indeed, our estimate indicates that ^{14}N relaxation is 5 orders of magnitude faster than the observed water-^1H relaxation (Fig. 1).

Any QP model based on fast ^{14}N relaxation requires a mechanism for polarization transfer from ^1H to ^{14}N. The only plausible candidate is an energy-conserving flip–flop transition induced by a ^1H–^{14}N dipole coupling [3,9]. This mechanism is only effective at magnetic field strengths where the ^1H Zeeman splitting matches one of the three ^{14}N splittings, thus accounting for the observed Q-peak frequencies.

4.2. The amide proton

Since ^{14}N has a small magnetic moment, only the directly attached amide proton can produce a dipole coupling of the required strength. To conclusively demonstrate that the amide proton is a necessary ingredient in the QP mechanism, we measured the Q peaks from BPTI in H_2O/D_2O mixtures with the solvent proton fraction X_H varying from 0.2 to 1 (Fig. 4). Prior to measurements, the samples were equilibrated for 10–12 days. Although the most deeply buried amide hydrogens in BPTI exchange very slowly [30], all amide hydrogens close to intermediary protons (in internal waters or hydroxyl groups; see Sections 4.3 and 5.4) are equilibrated with the solvent during the 10–12 days that elapsed prior to measurements [31,32].

For the ^2H–^{14}N moiety, level crossing would occur at ^1H frequencies higher by a factor $\gamma(^1H)/\gamma(^2H) = 6.51$ than the observed Q peaks and polarization transfer (at level crossing) would be a factor $[\gamma(^1H)/\gamma(^2H)]^2 = 42.4$ slower than for the ^1H–^{14}N moiety. Therefore, if the amide proton is a necessary part of the QP mechanism, deuterated amide groups should not contribute significantly to the observed Q peaks. The integrated Q-peak intensity should then be proportional to the probability, P_{NH}, that the amide nitrogen is bound to a proton (rather than to a deuteron), while the Q-peak frequency and width should be independent of X_H. The latter predictions are confirmed by the data (Fig. 4a and c). Furthermore, as predicted, the integrated Q-peak intensities decrease towards zero as protons are removed from the solvent, but the intensity is a nonlinear function of X_H (Fig. 4b). Such a nonlinear dependence is indeed expected, since [51]

$$P_{NH} = \frac{X_H}{X_H + (1 - X_H)\phi_{NH}} \tag{8}$$

where the fractionation factor ϕ_{NH} is the equilibrium constant for the exchange reaction

$$NH + D(aq) \rightleftharpoons ND + H(aq) \tag{9}$$

Using Eq. (8) to fit to the X_H-dependence of the $Q_\pm$ peak intensities (Fig. 4b), we obtain $\phi_{NH} = 0.43 \pm 0.02$. This is in the range 0.28–1.47 reported for the protein staphylococcal nuclease [52,53]. Moreover, small ϕ_{NH} values are linked to strong hydrogen bonds [52,53] and the amide hydrogens that are close to intermediary protons are indeed strongly hydrogen-bonded (Section 5.4).

In conclusion, our analysis of the data in Fig. 4 demonstrates that the amide proton is an obligatory intermediate in the polarization transfer pathway leading from water protons to the lattice via amide ^{14}N nuclei.

4.3. Intermediary protons

Before addressing the quantitative aspects of relaxation in the NH spin system, we shall consider the preceding magnetization transfer from bulk water protons to the amide proton. The simplest mechanism for this step would be a direct exchange process. However, amide proton exchange is far too slow to account for the observed Q peaks. Clearly, R_1^Q cannot exceed the rate constant for magnetization transfer from water to amide protons, which is $(2N_W)^{-1}\sum_k \tau_{Ak}^{-1}$ with $N_W = 3000$ the water/protein mole ratio and τ_{Ak} the mean residence time of amide proton k. At 20 °C and pH 4.2, a fully solvent-exposed amide proton in poly-alanine [54] or in the flexible C-terminus of mUb [34] has $\tau_A \approx 1$ min. In folded proteins most amide protons are buried and internally hydrogen-bonded, so τ_A is orders of magnitude longer than for a fully exposed amide proton [30–32,34]. Direct amide proton exchange thus fails by several orders of magnitude to account for the Q peaks. Also, since amide proton exchange is base-catalyzed, we would expect larger Q peaks at higher pH, which is not observed (Fig. 3 and Table 2).

Since direct exchange is too slow, magnetization must be transferred to the amide proton by dipolar cross-relaxation or spin diffusion, either directly from water or as the last step in a magnetization transfer chain that may comprise several exchange or cross-relaxation/spin-diffusion steps. To determine if non-exchangeable protein protons are involved in the magnetization transfer pathway, we measured the Q peaks from normal mUb and from *d*-mUb, with 83% of the non-exchangeable protons substituted by deuterons. The insignificant effect of protein deuteration (Fig. 6 and Table 2) demonstrates that only labile protons (including water protons) are involved in the magnetization transfer pathway.

In order to enhance the water-^1H relaxation rate by ~1 s^{-1}, as observed, the rate of magnetization transfer from labile to amide proton must be of order $10^4\,s^{-1}$ since the effect is attenuated by the 'dilution factor' $(2N_W)^{-1}$. The dipolar cross-relaxation rate can have this magnitude only if the two protons are close in space and if their mutual dipole coupling is modulated on the microsecond time scale. We propose that this modulation is produced by exchange-mediated orientational randomization (EMOR) upon exchange of the labile proton. We refer to such labile protons, which reside near an amide proton and exchange on the microsecond time scale, as intermediary protons since they mediate the magnetization transfer from water to amide proton. Because only a few of the amide protons in a given protein are close to an intermediary proton, the Q-peak intensity is not proportional to the total number of amide protons, as previously assumed [18], but rather to the number of intermediary protons in the protein.

The intermediary protons must either belong to internal water molecules or to amino-acid side-chains with labile protons. Under our solution conditions, the only relevant labile protons are the hydroxyl protons in serine, threonine or tyrosine residues. The close agreement between the Q peaks from BPTI and mUb when normal-

ized to the same protein concentration (or N_W) must be coincidental. mUb contains 44% more amide protons than BPTI (88 versus 61), so the Q-peak intensity is clearly not proportional to the total amide proton (or amide nitrogen) concentration. BPTI contains 4 internal water molecules, two of which have residence times in the microsecond range [37] and reside within 3 Å of amide protons [28]. In contrast, the single internal water molecule in mUb [29] has a residence time of only 20 ns at 20 °C [37] and is therefore not a potent intermediary species. On the other hand, mUb has 7 hydroxyl protons within 3 Å of an amide proton, whereas BPTI only has 3. We thus attribute the Q-peaks to hydroxyl protons in mUb and to a combination of hydroxyl protons and internal-water protons in BPTI. In Section 5.4 we show that these predictions are quantitatively consistent with the data.

If intermediary protons are an integral part of the magnetization transfer pathway, it should be possible to find proteins that do not give rise to Q peaks. Gelatin gels are built from collagen-like triple-helical junction zones, 100–200 residues in length, connected by flexible single chains [55]. The regular collagen triple helix is densely packed and does not contain any internal water [56]. Water ^{2}H and ^{17}O MRD studies of gelatin gels do reveal some internal water molecules [48], presumably associated with structural defects, but these water molecules are too few and to short-lived (4–40 ns at 10 °C) to produce significant Q peaks. For the gelatin preparation used in this study, hydroxyl-bearing side-chains (including hydroxyproline) are present at roughly the same mole fraction as in mUb, but since all side-chains in gelatin are fully solvent-exposed [57] there are no long-lived conformations with a hydroxyl protein near an amide proton. On structural grounds, we thus expect that a gelatin gel should not give rise to significant Q peaks. This prediction is consistent with published ^{1}H MRD data from gelatin gels [58]. Because that study did not sample the QP region densely, we now report new ^{1}H data from a gelatin gel, clearly demonstrating that the Q peaks from gelatin are insignificant compared to those from BPTI and mUb at the same water content and pH (Fig. 7). A quantitative analysis of the gelatin data, as in Fig. 1, does reveal small Q peaks, but the combined integrated intensity of the $Q_\pm$ peaks (that is, $C_+ + C_-$) is only 4% of the values obtained for BPTI and mUb (Table 2). In contrast, large Q peaks have been reported from collagen fibers in tendon [16], but *in vivo* collagen triple helices build higher-order structures by lateral self-association [59] that may well contain internal water molecules with residence times in the microsecond range.

The requirement of intermediary protons also explains why no Q peaks have been observed at the frequencies (<1 MHz) corresponding to the ^{14}N quadrupole coupling of ammonium and guanidinium groups in lysine and arginine side-chains. Because these charged and flexible side-chains usually protrude into the solvent, an intermediary proton is not likely to remain in close proximity to one of the NH protons for as long as a microsecond.

5. Quantitative model

5.1. Magnetization transfer pathway

According to the QP model proposed here, the enhancement of the water-^{1}H relaxation rate at the three ^{14}N frequencies Ω_α can be described in terms of a magnetization transfer scheme (Fig. 8) featuring an intermediary proton (I), an amide proton (A) and $2N_W$ external water protons (W). The magnetization transfer pathway involves three consecutive steps. The mechanism of the first step is material exchange by water diffusion and/or chemical proton exchange. The rate constant for magnetization transfer from I to W is $1/\tau_I$, the inverse of the I-proton residence time. Detailed balance requires the rate constant of the reverse process to be $1/(2N_W\,\tau_I)$. The

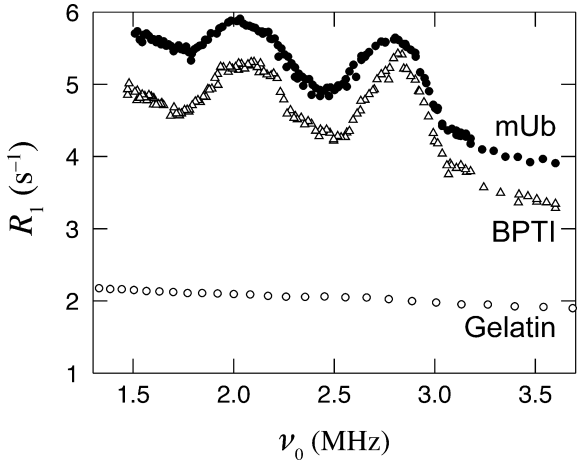

Fig. 7. Water-^{1}H relaxation rate from a gelatin gel at pH 5.3 and 10 °C (○) with barely visible Q peaks. Shown for comparison are the R_1 data for BPTI at pH 5.1 (△) and mUb at pH 5.3 (●), both at 20 °C, from which the Q peaks in Fig. 5 were derived. All three data sets have been normalized to 50 water molecules per amino acid residue.

intrinsic relaxation rate of the W protons is denoted R_W. In the second step, ^{1}H magnetization is transferred from I to A by dipolar flip–flop transitions, characterized by the cross-relaxation rate σ. This transfer competes with the back-exchange from I to W and with the auto-relaxation of the I proton, characterized by the rate ρ_I. In the last step, the A spin relaxes at a rate ρ_A that can be split in two parts:

$$\rho_A = \rho_{A0} + \rho_{AN} \tag{10}$$

Because of its fast quadrupolar relaxation, the ^{14}N spin is in thermal equilibrium with the lattice on the time scale of A-spin relaxation. There is thus no ^{1}H–^{14}N cross-relaxation in the sense of the Solomon equations [1] and the ^{14}N spin enters the model only via its contribution, ρ_{AN}, to the A-spin auto-relaxation rate ρ_A. This contribution is 'resonant' since it is significant only at the ^{1}H Larmor frequencies ω_0 where the ^{1}H Zeeman splitting matches one of the three ^{14}N splittings. We shall return to ρ_{AN} in Section 5.3.

Magnetization transfer among the W, I and A spins according to the scheme in Fig. 8 is described by three coupled differential equations:

$$\frac{dm_W}{dt} = -\left(R_W + \frac{1}{2N_W\tau_I}\right)m_W + \frac{1}{2N_W\tau_I}m_I \tag{11a}$$

$$\frac{dm_I}{dt} = -\left(\rho_I + \frac{1}{\tau_I}\right)m_I + \frac{1}{\tau_I}m_W - \sigma m_A \tag{11b}$$

$$\frac{dm_A}{dt} = -\rho_A m_A - \sigma m_I \tag{11c}$$

where $m_X \equiv (M_X - M_X^0)/M_X^0$ is the reduced longitudinal magnetization of spin X. The observed relaxation rate R_1 characterizes the decay of the W magnetization. Although Eq. (11) predicts a tri-exponential decay in general, the observed decay is mono-exponential within experimental accuracy. We can therefore identify R_1 with the integral relaxation rate

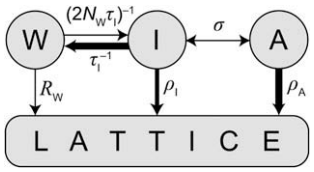

Fig. 8. Schematic view of the magnetization transfer pathway.

$$R_1 = \left[\int_0^\infty dt\ m_W(t)/m_W(0)\right]^{-1} \tag{12}$$

which can be obtained analytically from Eq. (11) as

$$R_1 = R_W + \frac{1}{2N_W\tau_I}\left[1 - \frac{\rho_A}{\rho_A(1+\rho_I\tau_I) - \sigma^2\tau_I}\right] \tag{13}$$

This result was obtained with the selective initial condition $m_X(0) = \delta_{XW}$, although the field-cycling experiments correspond to the nonselective initial condition $m_X(0) = 1$. However, the R_1 expressions resulting from these two initial conditions do not differ significantly in the dilute regime, where $2N_W >> 1$. For $\sigma = 0$, Eq. (13) reduces to the familiar two-state exchange formula in the dilute regime

$$R_1 = R_W + \frac{1}{2N_W} \times \frac{1}{\tau_I + 1/\rho_I} \tag{14}$$

According to Eqs. (1) and (10), the QP contribution to R_1 is given by

$$R_1^Q = R_1(\rho_A) - R_1(\rho_{A0}) \tag{15}$$

On substituting R_1 from Eq. (13), we find that R_1^Q can be expressed as the product of two functions:

$$R_1^Q(\omega_0) = \hat{R}(\omega_0)L(\omega_0) \tag{16}$$

with

$$\hat{R} = \frac{N_I}{2N_W} \times \frac{\sigma^2}{(1+\rho_I\tau_I)^2 R_{IA}} \tag{17}$$

$$L = \frac{\rho_{AN}}{\rho_{AN} + R_{IA}} \tag{18}$$

$$R_{IA} = \rho_{A0} - \frac{\sigma^2\tau_I}{1+\rho_I\tau_I} \tag{19}$$

The dimensionless shape function $L(\omega_0)$ determines the positions, widths and relative intensities of the three Q peaks, whereas the peak rate $\hat{R}$, corresponding to R_1^Q when $\rho_{AN} >> R_{IA}$, acts as an overall scaling factor that is essentially independent of frequency.

The preceding treatment pertains to the situation where the W protons exchange with a single I proton, but a protein generally contains several I protons. In the dilute regime, different I protons contribute additively so the total R_1^Q is obtained by summing the product $\hat{R}L$ over the N_I I protons. To limit the number of parameters in the model, we shall treat the I protons as a homogeneous group with effective values for the residence time τ_I and other microscopic parameters. This approximation has already been implemented in Eq. (17) by multiplying the peak rate for a single I proton by the number, N_I, of I protons in the protein.

5.2. Peak rate

To calculate the peak rate $\hat{R}$, we need to model the spectral density functions that determine the rates σ, ρ_I an ρ_{A0}. These rates are all dominated by the EMOR modulation of dipole couplings involving the I proton, with the residence time τ_I (in the microsecond range) as correlation time. It is convenient to single out the effects of the I–A dipole coupling by writing

$$\rho_I = \rho_{IA} + \rho_{IX} \tag{20}$$

$$\rho_{A0} = \rho_{IA} + \rho_{AX} \tag{21}$$

so that

$$\rho_{IA}(\omega_0) = \bar{\omega}_{D,IA}^2[0.1j_I(0) + 0.3j_I(\omega_0) + 0.6j_I(2\omega_0)] \tag{22}$$

$$\sigma(\omega_0) = \bar{\omega}_{D,IA}^2[0.6j_I(2\omega_0) - 0.1j_I(0)] \tag{23}$$

with the reduced spectral density function

$$j_I(\omega) = \frac{\tau_I}{1+(\omega\tau_I)^2} \tag{24}$$

and the residual dipole coupling constant

$$\bar{\omega}_{D,IA} = \frac{\mu_0}{4\pi}\frac{\hbar\gamma^2}{r_{IA}^3}S_{IA} \tag{25}$$

The term ρ_{IX} in Eq. (20) represents the contribution from all dipole couplings of I, except the one to A. These couplings are modulated by the exchange of the I spin so ρ_{IX} is governed by the same spectral density, Eq. (24), as ρ_{IA}. We can therefore write $\rho_{IX} = \lambda\ \rho_{IA}$, with

$$\lambda = \frac{1}{\bar{\omega}_{D,IA}^2}\sum_k \bar{\omega}_{D,Ik}^2 \tag{26}$$

The term ρ_{AX} in Eq. (21) represents the contribution from all dipole couplings of A, except the one to I. Because these couplings are modulated by restricted internal motions with correlation times much shorter than τ_I, we expect that $\rho_{AX} << \rho_{IA}$. We shall therefore set $\rho_{AX} = 0$. The peak rate is shown as a function of τ_I in Fig. 9.

If τ_I is in the microsecond range, $(\omega_0\tau_I)^2 >> 1$ at the MHz frequencies of the Q peaks so ρ_{IA} and σ in Eqs. (22) and (23) are completely dominated by the adiabatic spectral density $j_I(0)$. In this adiabatic limit, the peak rate in Eq. (17) is given by

$$\hat{R} = \frac{N_I}{2N_W\tau_I} \times \frac{\zeta}{(1+\lambda\zeta)[1+(1+\lambda)\zeta]} \tag{27}$$

where $\zeta = (\bar{\omega}_{D,IA}\tau_I)^2/10$. The peak rate $\hat{R}$ increases linearly with τ_I for small τ_I, passes through a maximum, and then decreases as τ_I^{-3} (Fig. 9). At the $Q_\pm$ frequencies, the approximate Eq. (27) does not differ significantly from the exact Eq. (17), but at the lower Q_0 frequency $\hat{R}$ is slightly overestimated by Eq. (27) for $\tau_I < 10$ μs. Considering that the proteins contain several I protons ($N_I > 1$), it is clear that the model can account for the observed R_1^Q values of $\sim 1\ s^{-1}$ at the $Q_\pm$ peaks, provided that shape function $L(\omega_0)$ in Eq. (18) is not much smaller than 1 at the peaks.

5.3. Shape function

To complete the model, we must specify the polarization transfer rate ρ_{AN} that governs the shape function $L(\omega_0)$ in Eq. (18). This process is driven by the residual dipole coupling (averaged by fast

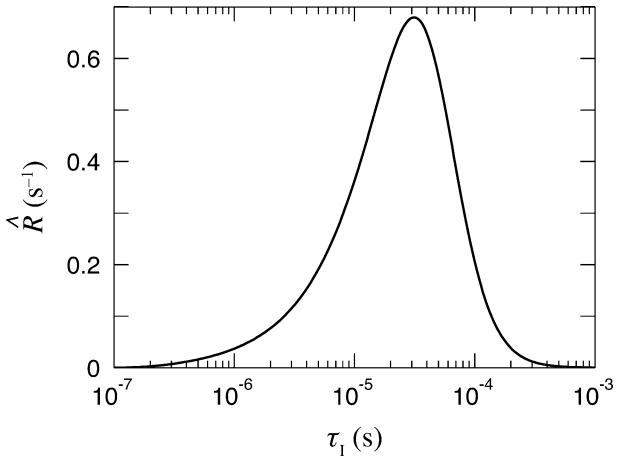

Fig. 9. Peak rate $\hat{R}$ at $\nu_0 = 2$ MHz versus the I-proton residence time τ_I, calculated from Eqs. (17)–(24) with $r_{IA} = 2.5$ Å, $\lambda = 1$, $N_I = 1$ and $N_W = 3000$.

internal motions) between the A proton and the ^{14}N spin in the amide N–H group,

$$\bar{\omega}_{D,AN} = \frac{\mu_0}{4\pi}\frac{\hbar\gamma(^1H)\gamma(^{14}N)}{r_{AN}^3}S_{AN} \tag{28}$$

This coupling is not modulated by the EMOR mechanism, because the residence time, τ_A, of the amide proton is many orders of magnitude longer than $1/\bar{\omega}_{D,AN} \approx 20$ μs (Section 4.3). Global restricted protein rotation modulates the A–N dipole coupling, just like it modulates the ^{14}N quadrupole coupling and the I–A dipole coupling, but since $\bar{\omega}_{D,AN}$ is a factor 500 smaller than ω_Q the dipolar relaxation rate induced by this motion is 5 orders of magnitude smaller than the quadrupolar relaxation rate, R_Q, in Eq. (7). While this nanosecond motion clearly cannot be responsible for ρ_{AN}, it contributes to the motional averaging of the residual dipole coupling $\bar{\omega}_{D,AN}$ via the order parameter S_{AN}.

As noted in Section 5.2, the shape function $L(\omega_0)$ must be of order 1 at the $Q_\pm$ peaks to account for the observed peak amplitudes. This means that ρ_{AN} at the peak must be at least comparable to R_{IA}, which is of order 10^3 s^{-1} (Section 5.2). Such a high rate can only be obtained if the A–N dipole coupling is modulated on the microsecond time scale. Since persistent motions of the protein backbone do not occur on this time scale, the only remaining possibility is that ρ_{AN} is governed by dipolar relaxation 'of the second kind', that is, the dipole coupling is averaged to zero by transitions in the ^{14}N spin system. This relaxation mechanism is well known in the context of paramagnetically enhanced ^{1}H relaxation, where $S \geq 1$ electron spin relaxation induced by modulation of the zero-field splitting (ZFS) plays the same role as quadrupolar ^{14}N relaxation does here [22]. The conventional Solomon–Bloembergen–Morgan treatment is valid in the high-field regime, where the Zeeman coupling is much larger than the ZFS [45]. Here we are in the opposite regime, where the static quadrupole coupling is larger than the ^{14}N Zeeman coupling. This regime has also been analyzed in the electron-spin ZFS context [39–45].

In Appendix A, we show that the resonant contribution to ρ_{AN} (the other contributions can safely be neglected) can be expressed as

$$\rho_{AN}(\omega_0) = \sum_\alpha \rho_{AN}^\alpha(\omega_0) \tag{29}$$

where the α sum runs over the three ^{14}N transitions (labeled 0, – and + as before), and

$$\rho_{AN}^\alpha(\omega_0) = \frac{2}{9}\bar{\omega}_{D,AN}^2 B_\alpha \frac{R_Q^\alpha}{(R_Q^\alpha)^2 + (\omega_0 - \Omega_\alpha)^2} \tag{30}$$

In general, the coefficients B_α, the ^{14}N frequencies Ω_α and the quadrupolar relaxation rates R_Q^α all depend on the orientation of the $\boldsymbol{B}_0$ field relative to the principal ^{14}N EFG frame, specified by the Euler angles $\Omega_{LF} = (-, \beta_{LF}, \gamma_{LF})$. Since all orientations are represented with equal probability in the sample, the observed Q-peak rate R_1^Q is an isotropic powder average. Accordingly, the shape function in Eq. (18) should be evaluated as

$$L(\omega_0) = \sum_\alpha L_\alpha(\omega_0) \tag{31}$$

with

$$L_\alpha(\omega_0) = \frac{1}{4\pi}\int_0^{2\pi} d\gamma_{LF}\int_{-1}^{1} d\cos\beta_{LF}\,\frac{\rho_{AN}^\alpha(\omega_0;\beta_{LF},\gamma_{LF})}{\rho_{AN}(\omega_0;\beta_{LF},\gamma_{LF}) + R_{IA}(\omega_0)} = \left\langle \frac{\rho_{AN}^\alpha}{\rho_{AN} + R_{IA}} \right\rangle \tag{32}$$

where ρ_α in the denominator is the sum in Eq. (29).

For the quantitative data analysis, the ^{14}N frequencies Ω_α were computed numerically by diagonalizing the static ^{14}N spin Hamiltonian (Appendix A). The simple expressions in Eqs. (3) and (5) are only valid in the low-field regime, when $\omega_{0,N}$ is small compared to $\bar{\omega}_Q$. As seen from Fig. 10, this approximation is not quantitatively accurate. We neglect the orientation dependence of the quadrupolar relaxation rates, but we allow for a spin-state dependence by stipulating that $R_Q^\pm = R_Q$ and $R_Q^0 = \mu R_Q$, with R_Q and μ treated as model parameters. For a given R_Q, Eq. (7) may be used to estimate the associated correlation time, τ_Q.

The coefficients B_α were computed numerically from Eqs. (A20) and (A24). In the low-field regime, approximate analytical expressions can be derived for B_α, see Eq. (A26). As a further approximation, one may pre-average these expressions over the Ω_{LF} distribution so that the powder average in Eq. (32) only involves the frequencies Ω_α. We then obtain

$$\langle B_\pm \rangle = 1 + \frac{3}{2}\sin^2\beta_{FD}[1 \pm \cos(2\alpha_{FD})] \tag{33a}$$

$$\langle B_0 \rangle = 1 + 3\cos^2\beta_{FD} \tag{33b}$$

where α_{FD} and β_{FD} are the spherical polar angles that specify the orientation of the N–H bond with respect to the principal frame of the ^{14}N EFG tensor. According to this approximate result, α_{FD} affects the relative intensity of the Q_+ and Q_- peaks, whereas β_{FD} affects the intensity of Q_0 relative to $Q_\pm$.

As seen from Fig. 11, the low-field approximation yields a quite accurate lineshape function, although the peaks are slightly downshifted in frequency. As expected, the shift is most noticeable for the highest-frequency Q_+ peak. However, pre-averaging of the B_α coefficients leads to a significant overestimate of the Q_+ intensity. The absolute integrated intensity, I_α, of the shape function for peak Q_α is obtained from Eqs. (30) and (32) by noting that R_{IA} can be regarded as a constant over the frequency range of the Q peak (Section 5.1):

$$I_\alpha \equiv \int_{-\infty}^{\infty} d\omega_0 L_\alpha(\omega_0) = \frac{2\pi\bar{\omega}_{D,AN}^2}{9R_{IA}}\left\langle B_\alpha\left(1 + \frac{2\bar{\omega}_{D,AN}^2 B_\alpha}{9R_{IA}R_Q^\alpha}\right)^{-1/2}\right\rangle \tag{34}$$

For sufficiently large R_Q, I_α is thus proportional to $\langle B_\alpha \rangle$. However, for the (representative) parameter values used in Fig. 11, the second term within parentheses in Eq. (34) is of order 1, which ac-

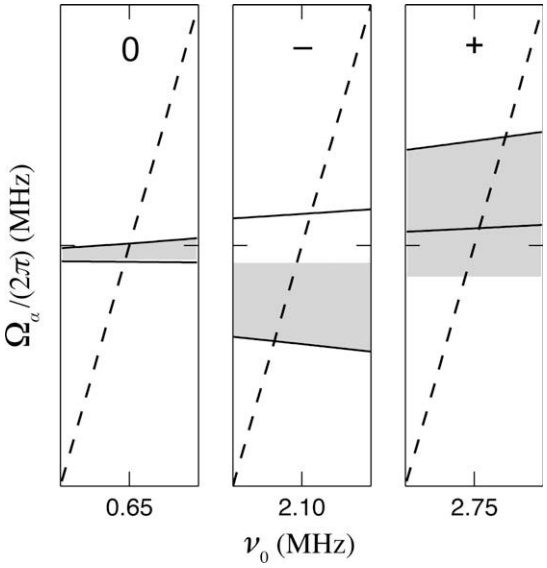

Fig. 10. ^{14}N frequencies Ω_0, Ω_- and Ω_+ (from left to right), computed exactly by numerical diagonalization and from the low-field formula (3), versus ^{1}H Larmor frequency, ω_0. The Ω_{LF}-dependent range of Ω_α values is bounded by the two curves (exact) or indicated by the shaded region (low-field approximation). Each panel depicts 200 × 200 kHz and the dashed line is $\Omega_\alpha = \omega_0$. Parameter values: $\bar{\nu}_Q = 3.22$ MHz, $\eta = 0.4$, $\alpha_{FD} = 30°$ and $\beta_{FD} = 90°$.

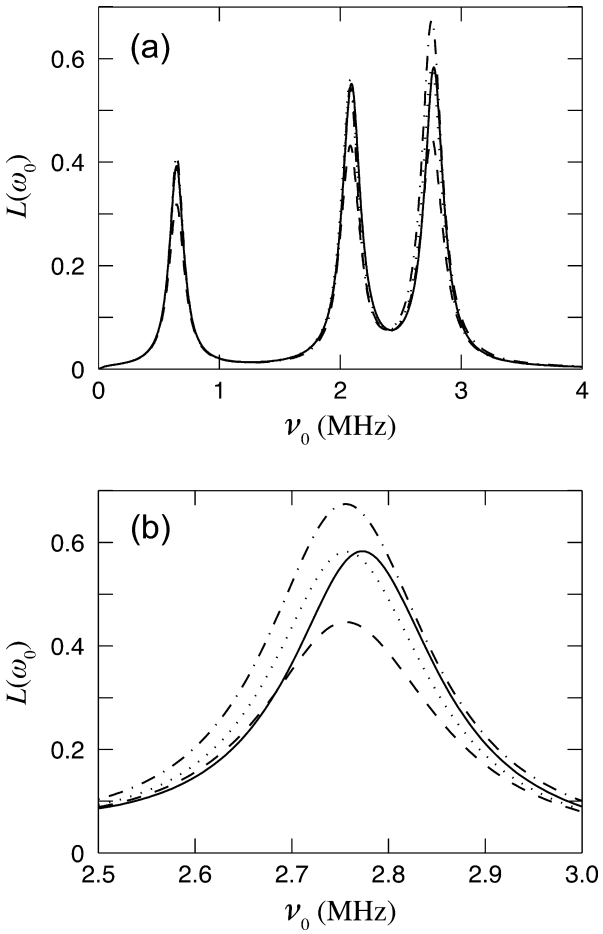

Fig. 11. (a) Shape function $L(\omega_0)$ computed without approximations (solid curve), with the low-field approximation (dotted), and with the low-field approximation and pre-averaged B_α coefficients (dash-dotted). The dashed curve was calculated from a spin-temperature approach in the low-field approximation (Appendix A). (b) Enlargement of the Q_+ peak. Parameter values: $\bar{\nu}_Q = 3.22$ MHz, $\eta = 0.4$, $\alpha_{FD} = 30°$, $\beta_{FD} = 90°$, $\bar{\omega}_{D,AN} = 4.89 \times 10^4\ s^{-1}$, $1/R_Q = 3$ μs, $\mu = 1$, $R_{IA} = 2280\ s^{-1}$ (corresponding to $r_{IA} = 2.5$ Å, $\lambda = 1$ and $\tau_I = 10$ μs).

counts for the deviation of the dash-dotted curve in Fig. 11. Since $\hat{R}$ is essentially independent of ω_0 in the QP range, the observed integrated Q-peak intensity is given by

$$C_\alpha = \hat{R}(\Omega_\alpha) I_\alpha(\Omega_\alpha) \tag{35}$$

For an order-of-magnitude estimate, we use Eq. (27) (adiabatic limit) with $\lambda\ \zeta << 1$ (for τ_I less than the maximum in Fig. 9) and we neglect the second term in Eq. (34) (which requires that R_Q is not too small). With these approximations,

$$C_\alpha \approx \frac{\pi}{9} \frac{N_I}{N_W} \bar{\omega}_{D,AN}^2 \langle B_\alpha \rangle \tag{36}$$

The last two factors in this expression are determined by the essentially invariant properties of the amide group: the bond length r_{AN}, the bond order parameter S_{AN}, and the orientation of the EFG tensor in the molecule frame (α_{FD}, β_{FD}). As long as τ_I and τ_Q are in the plausible broad ranges assumed in the derivation, the Q-peak intensity C_α is independent of dynamic parameters. It should therefore not depend much on temperature, in accord with our observations (Fig. 2b). The intensity C_α is inversely proportional to the water content (N_W), as demonstrated previously [18] and as is also evident from our raw data (before N_W scaling). The critical parameter that accounts for the variation of Q-peak intensity among different proteins is the number, N_I, of intermediary protons. For BPTI and mUb, N_I is in the range 5–10. With $N_W = 3000$, $\bar{\omega}_{D,AN} = 4.89 \times 10^4\ s^{-1}$, $\alpha_{FD} \approx 30°$ and $\beta_{FD} \approx 90°$, Eqs. (33a) and (36) yield $C_+ \approx 1$ MHz s^{-1}, which is consistent with our data (Table 2).

We now consider the width of the Q peaks. According to Eqs. (30) and (32), $L_\alpha(\omega_0)$ is a Lorentzian with (FWHM) linewidth

$$\Delta_\alpha = 2R_Q^\alpha \left(1 + \frac{2\bar{\omega}_{D,AN}^2 B_\alpha}{9 R_{IA} R_Q^\alpha}\right)^{1/2} \tag{37}$$

In addition to this homogeneous broadening, the orientation dependence of the frequency Ω_α adds ~50 kHz (Fig. 10) inhomogeneous broadening for $Q_\pm$ (and less for Q_0). To explain the observed $Q_\pm$ linewidths of ~400 kHz (Table 2) with homogeneous broadening according to Eq. (37), we need $1/R_Q = 0.8$ μs. Such a short quadrupolar relaxation time seems unlikely in view of Eq. (7). Furthermore, if the observed linewidth were of a purely homogeneous origin, the Q peaks would be Lorentzian. However, the Q peaks are more nearly Gaussian than Lorentzian (Fig. 1). Even more decisively, Eqs. (7) and (37) imply that the linewidth should be a strongly decreasing function of temperature. With an activation energy of 20 kJ mol^{-1} for τ_Q (a low estimate), the linewidth should decrease by a factor 4 over the temperature range examined in Fig. 2c, whereas no significant temperature variation is observed.

These considerations lead us to conclude that the Q-peak width is predominantly of inhomogeneous origin. Specifically, we propose that a Gaussian distribution of the order parameter S_Q, and thus of the residual quadrupole coupling $\bar{\omega}_Q$, see Eq. (4), results from spatial variation in the degree and topology of intermolecular crosslinks within the disordered protein gel. The shape function $L_\alpha(\omega_0)$ in Eq. (32) should then be averaged over the distribution

$$f(\bar{\omega}_Q) = \left(2\pi\sigma_Q^2\right)^{-1/2} \exp\left[-\frac{1}{2}\left(\frac{\bar{\omega}_Q - \bar{\omega}_Q^0}{\sigma_Q}\right)^2\right] \tag{38}$$

As we shall see, the observed Q-peak widths can be explained by as little as ~5% relative variation in $\bar{\omega}_Q$. We specify the relative HWHM width of the distribution by the parameter, $\delta_Q \equiv (2\ln 2)^{1/2} \sigma_Q / \bar{\omega}_Q^0$.

5.4. Model parameters

The model parameters can be divided in two groups. Parameters associated with the ^{14}N quadrupole coupling and its modulation determine the position, width, shape and relative intensity of the Q peaks. Parameters associated with the dipole couplings of the intermediary (I) and amide (A) protons and the modulation of these couplings determine the absolute intensity of the Q peaks. In fitting the model to the Q-peak data, we used the most general version of the model (Appendix A), with numerical diagonalization of the static ^{14}N spin Hamiltonian (without assuming low-field conditions) and numerical averaging of the shape function over the Ω_{LF} and $\bar{\nu}_Q$ distributions. Fits based on the low-field version of the model yield significant differences in only two parameters: $\bar{\nu}_Q$ is lower by 15 kHz, consistent with the results in Fig. 11, and α_{FD} is larger by ~15°. As seen from Figs. 12 and 13, the model accounts almost quantitatively for the observed frequencies, relative and absolute intensities, widths and shapes of the Q peaks measured on crosslinked BPTI and mUb. As the last step of our analysis, we now examine whether the parameter values obtained from these fits (Table 3) are consistent with independent information about ^{14}N quadrupole couplings in amide groups and about the structure and dynamics of BPTI and mUb.

The frequencies Ω_α, and thus the Q-peak positions, are determined by the static residual ^{14}N quadrupole coupling parameters $\bar{\nu}_Q$ and η (Appendix A). The fits yield essentially the same quadrupole coupling parameters for all samples: $\bar{\nu}_Q = 3.23 \pm 0.02$ MHz and $\eta = 0.41 \pm 0.01$. As already seen from the preliminary analysis (Sec-

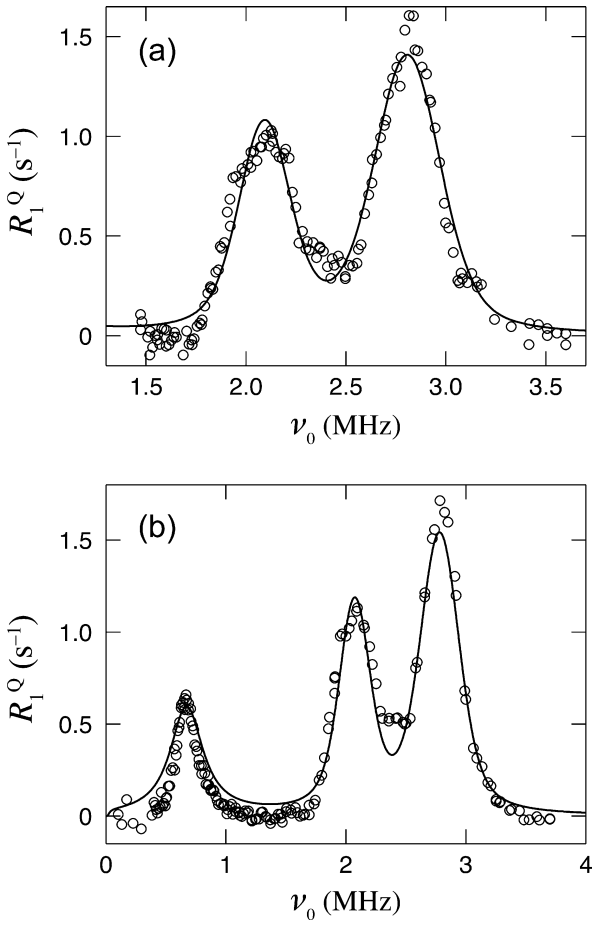

Fig. 12. Model fits to Q peaks from BPTI at (a) pH 5.1 and 20 °C (sample B2) and (b) at pH 4.3 and 10 °C (sample B3).

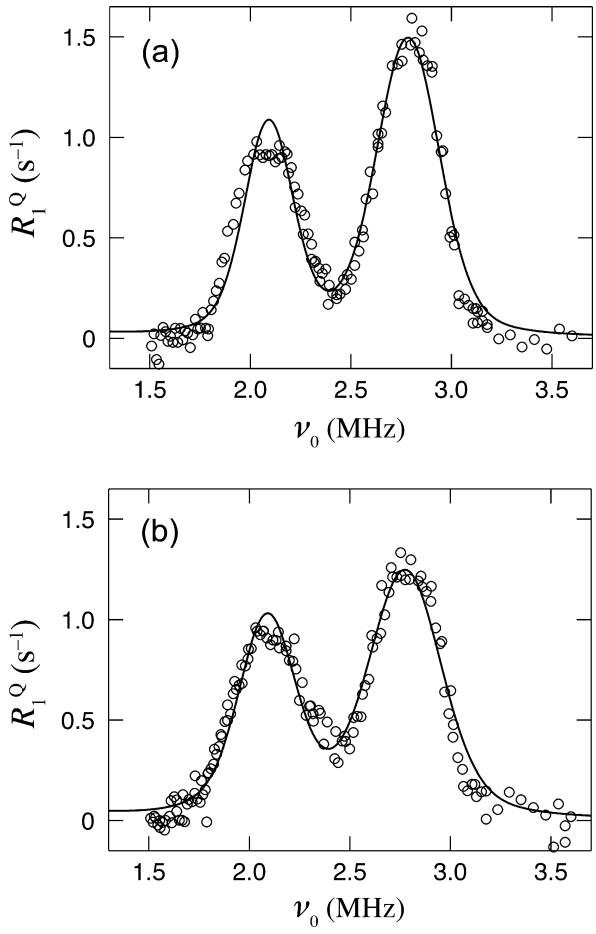

Fig. 13. Model fits to Q peaks from (a) mUb and (b) *d*-mUb, both at pH 5.3 and 20 °C.

tion 4.1), these values are consistent with the quadrupole parameters obtained from NQR studies of oligopeptide crystals [24]. For example, for the three peptide groups in tetra-glycine $\bar{\nu}_Q$ = 3.20–3.48 MHz and η = 0.37–0.42 [24]. With a global order parameter S_G = 0.88, as deduced from the temperature dependence of the peak positions (Section 4.1), Eq. (4) yields a rigid-lattice quadrupole coupling ν_Q = 3.27/0.88 = 3.72 MHz, somewhat larger than the NQR values for crystalline tetra-glycine. Presumably, there is some motional averaging also in the crystal, in addition to electrostatic perturbations from the charged end groups of the zwitterionic oligopeptide.

The shape of the Q peaks is determined by the width, σ_Q, of the Gaussian $\bar{\nu}_Q$ distribution (38) and by the ^{14}N quadrupolar relaxation rate, R_Q. These parameters depend on sample characteristics, such as the degree and heterogeneity of intermolecular crosslinks, and their values are not known a priori. All samples yield similar relative halfwidths of 5–6% for the assumed Gaussian $\bar{\nu}_Q$ distribution. If this spread is attributed to the global order parameter, it corresponds to a variation of 0.05 in S_G around its mean value of 0.88. Even such a small variation has a dominant effect on the width and shape of the Q peaks because the quadrupole coupling is large.

The relative integrated peak intensity is largely determined by the angles α_{FD} and β_{FD} of the N–H bond relative to the principal frame of the ^{14}N EFG tensor. Experimental and theoretical studies of small peptides show that the axis of the largest principal EFG component is perpendicular to the N–H bond, so that β_{FD} = 90° [24,60–63]. Some studies conclude that the axis of the smallest principal EFG component is close to the N–H bond [60], so that $\alpha_{FD} \approx 0$, while other studies have reported values of 30° [24] or 13° [63] for this angle. It is not clear if these differences reflect methodological limitations or real variations. In the fits, β_{FD} was fixed at 90° while α_{FD} was treated as an adjustable parameter. The resulting α_{FD} values, in the range 15–20°, are consistent with previous estimates. The significantly larger α_{FD} angle for *d*-mUb as compared to mUb (Table 3), which according to Eq. (33a) accounts for the smaller intensity difference between the Q_+ and Q_- peaks for the deuterated protein (Fig. 13), may be a genuine isotope effect on the orientation of the EFG tensor.

Table 3
Parameter values from model fits to Q-peak data.[a]

Parameter	BPTI (B2)	BPTI (B3)	mUb (U1)	*d*-mUb (U2)
ν_Q (MHz)	3.246(4)	3.216(5)	3.231(3)	3.223(4)
η	0.415(3)	0.416(3)	0.403(3)	0.401 (4)
δ_Q (%)	5.5(4)	5.2(5)	5.6(4)	6.2(5)
α_{FD} (°)[b]	18(1)	19(1)	16(1)	20(1)
R_Q^{-1} (μs)	2.8(1.0)	2.2(4)	3.8(1.5)	2.6(1.3)
$\bar{N}_l$[b]	4.3(1)	4.9(1)	4.2(1)	4.1(1)

[a] Data at 20 °C comprising the $Q_\pm$ peaks in all cases except BPTI (sample B3), where all three Q peaks measured at 10 °C were fitted. Uncertainty in the last digit (one standard deviation) given within parentheses.
[b] From fit based on Eq. (38).

The ^{14}N quadrupolar relaxation time, $1/R_Q$ = 3 ± 1 μs, does not differ significantly between the two proteins or among different samples. Inserting this R_Q value, $\bar{\nu}_Q$ = 3.23 MHz and S_G = 0.88 into Eq. (7), we obtain for the correlation time τ_Q = 7.4 ± 2.5 ns, which

is of the order-of-magnitude expected for restricted rotational diffusion of the flexibly crosslinked proteins.

The 'dipole parameters' mainly influence the absolute integrated intensity of the Q peaks via the peak rate $\hat{R}$ and via the effective rate R_{IA} that determines the maximum value of the shape function L_∞. Because the main effect of these parameters is a uniform scaling of the Q peaks, they can be approximately combined into a single effective parameter. To find this composite parameter, we first note that for the microsecond τ_I values of interest, $(\omega_0\tau_I)^2 >> 1$ so that $\hat{R}$ and R_{IA} are in the adiabatic limit; cf. Eq. (27). Under the stronger condition that τ_I is significantly longer than ~10 μs, we expect that R_{IA} is significantly larger than ρ_{AN} even at the peaks. Then Eqs. (16)–(19) yield the approximate result

$$R_1^Q(\omega_0) = \frac{\omega_{D,AN}^2}{2N_W}\tilde{N}_I\langle\langle\bar{\rho}_{AN}(\omega_0)\rangle\rangle \tag{39}$$

where $\omega_{D,AN}$ is given by Eq. (28) with $S_{AN} = 1$, $\bar{\rho}_{AN}(\omega_0) = \rho_{AN}(\omega_0)/\bar{\omega}_{D,AN}^2$ is given by Eqs. (29) and (30), the double angular brackets signify averaging over the Ω_{LF} and $\bar{\nu}_Q$ distributions, and

$$\tilde{N}_I = N_I\left[\frac{S_{AN}}{1+\lambda(\bar{\omega}_{D,IA}\tau_I)^2/10}\right]^2 \tag{40}$$

The first factor in Eq. (39) is determined by the known quantities N_W (=3000 here) and r_{AN} (=1.01 Å) and the last factor, $\langle\langle\bar{\rho}_{AN}(\omega_0)\rangle\rangle$, is determined by the 'quadrupole parameters' $\bar{\nu}_Q$, η, σ_Q, α_{FD}, β_{FD} and R_Q. All the 'dipole parameters' (N_I, r_{IA}, S_{IA}, S_{AN}, λ and τ_I) combine into the single effective parameter $\tilde{N}_I$, which acts as a frequency-independent scaling factor. Because the quantity within square brackets in Eq. (40) is <1, $\tilde{N}_I$ constitutes a lower bound on the number, N_I, of intermediary protons in the protein.

The fits shown in Figs. 12 and 13 were performed with the exact model, without any assumptions about τ_I. However, to obtain a convergent fit, only N_I and τ_I were adjusted while the remaining 'dipole parameters' were fixed. Even so, N_I and τ_I cannot be determined with useful accuracy because of their large covariance. When only two Q peaks are fitted, these two parameters also covary with α_{LF}. To extract meaningful information about N_I and τ_I, we therefore used Eq. (39). The values of $\tilde{N}_I$ and α_{LF} quoted in Table 3 were obtained in this way. The values of the other parameters in Table 3 did not differ significantly from those obtained with the full model and the fitted curves were indistinguishable. The single fit that includes the Q_0 peak (Fig. 12a) also involves the parameter μ, for which the fit (to the full model) yields 2.2 ± 0.4.

As the final test of the proposed QP model, we now show that intermediary protons of the required numbers and with the required properties are indeed present in BPTI and mUb. For mUb, where the single internal water molecule is too short-lived to contribute significantly to the Q peaks (Section 4.3), the I protons must be labile protons in protein side-chains. The carboxyl protons have submicrosecond residence times at 20 °C [64], making their contribution negligibly small, and, in any case, the 11 carboxyl groups in mUb are >90% deprotonated at pH 5.3 [65]. Ubiquitin contains 11 hydroxyl protons in serine (3), threonine (7) and tyrosine (1) side-chains. According to the crystal structure [29] (with hydrogens added in standard geometry), five of these 11 hydroxyl protons reside within 2.4 Å of at least one backbone amide proton (Thr-7, Thr-9, Thr-55, Tyr-59 and Ser-65) and two more are within 2.8 Å (Ser-20 and Thr-22). A quantitative analysis of the background water-^{1}H dispersion profile, $R_1^0(\omega_0)$, from the same mUb samples as examined here indicates that the residence time, τ_I, of the hydroxyl protons is of order 10–100 μs at 20 °C [46]. Because this is two orders of magnitude shorter than expected [33] for catalysis by H_3O^+ ions at pH 5.3, it was concluded that hydroxyl proton exchange in this sample is catalyzed mainly by acidic glutaraldehyde reaction products and, to a lesser extent, by the buffer [46]. The fits in Fig. 13 yield τ_I values of order 10^{-5} s, consistent with the values deduced from the background dispersion although the strong covariance with N_I introduces a large uncertainty. For such τ_I values, the 'adiabatic approximation', Eqs. (39) and (40), should be reasonably accurate, so we can use the $\tilde{N}_I$ values in Table 3 to estimate N_I. With $\tau_I = 30$ μs, $S_{AN} = S_{IA} = S_G = 0.88$, $\lambda = 0.5$ and $r_{IA} = 2.3$ Å (as obtained from a typical fit), we obtain from Eq. (40) and Table 3: $N_I \approx \tilde{N}_I/0.6 \approx 7$. Considering the approximations involved, this estimate is certainly consistent with our assignment of 7 hydroxyl protons as the intermediary protons responsible for the Q peaks from mUb.

BPTI has 8 hydroxyl protons, 3 of which are within 3 Å of a backbone amide proton (Tyr-35, Ser-47 and Thr-54) [28]. We would thus expect smaller Q peaks from BPTI than from mUb, but they are, in fact, very similar (Fig. 5). However, BPTI has four internal water molecules, two of which have residence times in the μs range [37] and at least one amide proton within 3 Å. The two proteins thus contain a similar number of I protons and should therefore, to first order, yield Q peaks of similar intensity [cf. Eq. (36)]. However, the quantitative analysis of the Q peaks from BPTI is complicated by the presence of two types of I protons with significantly different residence times. This complication may explain the somewhat inferior fits obtained for BPTI as compared to mUb. The dependence of the Q peaks on the residence time τ_I is subtle. For a homogeneous class of I protons, we expect the Q-peak intensity to exhibit a weak maximum as a function of τ_I. The apparent pH dependence for BPTI (Fig. 3 and Table 2) is probably caused by the buffer present at pH 5.1 but not at pH 4.2 (Table 1) giving a shorter hydroxyl τ_I at pH 5.1. Further, the complex temperature dependence of the Q-peak intensity from BPTI, featuring not only the expected maximum but also a minimum (Fig. 2b), may be attributed to the two classes of I protons (hydroxyl protons and internal-water protons) in BPTI giving rise to two distinct maxima. A further complication for BPTI, which we have not attempted to incorporate in the model, is the presence of dipole couplings among the different internal-water protons.

6. Conclusions

In this study, we have presented an extensive set of Q-peak data from crosslinked BPTI and mUb and developed a relaxation model that accounts quantitatively for the data in terms of the structure and dynamics of these well-characterized proteins. In the following, we summarize the salient features of our Q-peak model, indicating similarities and differences with previous treatments.

Magnetization transfer from bulk water to amide protons is not a direct process, but proceeds in two steps via intermediary protons in internal water molecules or side-chain hydroxyl groups. Efficient magnetization transfer relies on two critical properties of the intermediary proton: it resides near (<3 Å) at least one amide proton and it has a residence time in the microsecond range (1–100 μs). Importantly, the exchange of the intermediary proton is responsible for *both* magnetization transfer steps. In the first step, bulk-water magnetization is transferred to the intermediary proton via molecular diffusion coupled to intermittent protein conformational fluctuations (internal water molecules) or via diffusion and acid-catalyzed proton exchange (hydroxyl protons). In the second step, the residence time of the intermediary proton becomes the correlation time for dipolar cross-relaxation with the nearby amide proton. This mechanism of exchange-mediated orientational randomization (EMOR) of ^{1}H–^{1}H dipole couplings is also responsible for the background (non-resonant) ^{1}H relaxation dispersion [58,66], but a larger subset of the internal water molecules and labile protons are then active since there is no requirement of

proximity to amide protons. For the EMOR mechanism, full motional narrowing (of the dipole coupling) requires fast exchange. When the residence time of the intermediary proton becomes much longer than the inverse dipole coupling (~20 μs), cross-relaxation no longer yields effective magnetization transfer to the amide proton. In the dilute regime ($N_W >> 1$), this breakdown of the motional-narrowing condition is (approximately) captured by the model [58,66,67].

Previous authors have either ignored the magnetization transfer from bulk water to the amide proton [21,23] or assumed fast-exchange conditions [13,15]. Whereas Kimmich et al. did not specify the mechanism for this exchange [13], Koenig proposed a model similar to ours but with the important difference that he identified the intermediary protons as water molecules at the protein surface with a residence time of 0.3 ns [15]. With such a short residence time, a large number of intermediary protons is required to account for the observed Q-peak intensity and Koenig assumed that all amide groups are solvent-exposed with an adjacent 0.3 ns water molecule. However, we now know that nearly all water molecules in contact with the external protein surface have much shorter residence times [38,68]. Furthermore, even if the residence time were in the nanosecond range, EMOR-induced cross-relaxation would be in the motional-narrowing (fast-exchange) regime where the Q-peak intensity should decrease strongly with increasing temperature, contrary to observation. Finally, Koenig's model with interfacial intermediary protons does not, like our model, explain the near absence of Q peaks from gelatin gels.

The last step in the polarization transfer scheme is the relaxation of the amide proton by dipolar relaxation 'of the second kind', where the ^{1}H–^{14}N dipole coupling is modulated by ^{14}N spin fluctuations on the microsecond time scale. Our analysis indicates that the ^{14}N spin relaxation time is ~3 μs, which is short compared to the inverse ^{1}H–^{14}N dipole coupling (~20 μs) so the motional-narrowing approximation is valid. An alternative, essentially equivalent picture of the resonant dipolar relaxation of the amide proton is a coherent polarization transfer from the amide proton to the rapidly relaxing ^{14}N nucleus. In contrast to our model, previous authors have argued that the relaxation of the amide proton is driven by restricted fluctuations in the polypeptide backbone [9,11,13,14] or by slow isotropic protein tumbling [21,23]. However, at least in the model systems investigated here, those processes do not occur on the required microsecond time scale. Koenig did invoke dipolar relaxation 'of the second kind', but did not present a rigorous treatment of this mechanism [15]. Rather, he proposed a modification of the Bloembergen–Solomon–Morgan theory [45], which incorrectly predicts that all three Q peaks have the same intensity. Moreover, this *ad hoc* theory predicts Lorentzian Q peaks with a linewidth (FWHM) given by R_Q/π. However, the lineshape is more Gaussian than Lorentzian and the linewidth is insensitive to temperature and a factor ~4 larger than the homogeneous width of ~100 kHz corresponding to $1/R_Q \approx 3$ μs, as indicated by our analysis. These considerations lead us to conclude, as did Kimmich et al. [13], that the Q-peak width is dominated by inhomogeneous broadening associated with a distribution of the (residual) ^{14}N quadrupole coupling. In a randomly crosslinked protein gel, it is natural to associate this distribution with the global order parameter S_G, but a contribution to σ_Q from intrinsic geometry-dependent variations in the EFG tensor cannot be excluded.

The model developed and tested here accounts for the origin of Q peaks in water-rich biological materials, such as our model systems and most biological cells and tissues. Q peaks are also observed from biological materials with very low water content, such as lyophilized protein powders [9,11,13], in which case the measured ^{1}H relaxation rate pertains to the protein proton magnetization. The model presented here is not directly applicable under such conditions, where ^{1}H–^{1}H spin diffusion within the protein may play a role and the mechanism of ^{14}N quadrupolar relaxation may differ from the one proposed here. However, in water-rich systems, magnetization transfer pathways involving nonlabile protein protons are not important, as demonstrated by the insignificant effect of H → D substitution in the protein. For partially hydrated protein powders and other low-water systems, the mechanism described here may still be dominant, but the intermediary protons are then augmented by water molecules trapped at protein–protein interfaces which may have residence times in the microsecond range [69].

The main implications of the present work for potential applications of the QP phenomenon in cell biology and diagnostic medicine stem from our identification of the intermediary protons. First, since only a small subset of all amide protons are close to an intermediary proton, the Q-peak intensity is proportional to the concentration of intermediary protons rather than to the concentration of amide groups. Second, the number of intermediary protons is governed not only by the protein structure, but also by solution conditions, notably the presence of proton-exchange catalysts.

Acknowledgments

We thank Per-Olof Westlund for a critical reading of the manuscript and Bayer Healthcare AG for a generous supply of BPTI. This work was supported by the Swedish Research Council, the Knut & Alice Wallenberg Foundation and the Crafoord Foundation.

Appendix A

Here we present explicit results for the relaxation rate, ρ_{AN}, of the amide proton, induced by its dipole coupling with the covalently attached ^{14}N spin. This coupling is modulated by transitions among the ^{14}N states, induced by the ^{14}N residual quadrupole coupling, which, in turn, is modulated by restricted protein rotation. Essentially the same result for ρ_{AN} can be obtained by three different theoretical approaches. We consider first the most general of these approaches, which has been used previously to analyze ^{1}H relaxation induced by a dipole coupling to an electron ($S = 1$) spin relaxed by a static ZFS interaction [39]. Throughout Appendix A, the amide ^{1}H and ^{14}N spins are denoted by I and S, respectively. Note that the symbols I and A in the main text refer to the intermediary and amide proton, respectively.

The relevant part of the spin Hamiltonian is partitioned as

$$H = H_I + H_S + H_{IS} = H_I + H_S^{(0)} + H_S^{(1)} + H_{IS} \tag{A1}$$

The I-spin Hamiltonian is simply the Zeeman coupling,

$$H_I = \omega_0 I_Z^{(L)} \tag{A2}$$

where ω_0 is the ^{1}H Larmor frequency. The static S-spin Hamiltonian comprises the Zeeman coupling and the residual ^{14}N electric quadrupole interaction,

$$H_S^{(0)} = \omega_S S_Z^{(L)} + \frac{\bar{\omega}_Q}{4}\left[3S_Z^{2(F)} - 2 + \frac{\eta}{2}\left(S_+^{2(F)} + S_-^{2(F)}\right)\right] \tag{A3}$$

Here, ω_S is the ^{14}N Larmor frequency, $\bar{\omega}_Q$ is the residual quadrupole coupling constant and η is the asymmetry parameter of the electric field gradient (EFG) tensor at the ^{14}N nucleus. The superscripts L and F indicate that the spin operator components are expressed in the lab frame or in the principal frame of the EFG tensor, respectively. The term $H_S^{(1)}$ in Eq. (A1) is the fluctuating part of the quadrupole coupling, responsible for ^{14}N relaxation. The last term in Eq. (A1) is the ^{1}H–^{14}N dipole coupling

$$H_{IS} = -\sqrt{6}\bar{\omega}_{\mathrm{D,AN}} \sum_{M=-2}^{2} T^{(\mathrm{L})}_{2,M}(IS) D^{2}_{M0}(\Omega_{\mathrm{LD}}) \tag{A4}$$

with the residual dipole coupling constant $\bar{\omega}_{\mathrm{D,AN}}$ given by Eq. (28). Further, $D^{2}_{M0}(\Omega_{\mathrm{LD}})$ are rank-2 Wigner functions, Ω_{LD} are the Euler angles transforming from the lab frame to the dipolar frame D (with the Z_{D} axis along the N–H bond), and $T^{(\mathrm{L})}_{2,M}(IS)$ are normalized irreducible spherical two-spin tensor components. The latter can be decomposed in terms of single-spin operators as

$$T^{(\mathrm{L})}_{2,M}(IS) = (-1)^{M}\sqrt{5} \sum_{N=-1}^{1} \begin{pmatrix} 1 & 1 & 2 \\ N & M-N & -M \end{pmatrix} I^{(\mathrm{L})}_{1,N} S^{(\mathrm{L})}_{1,M-N} \tag{A5}$$

It is convenient to transform the S-spin operators and the Wigner functions from the lab frame (L) to the principal frame (F) of the ^{14}N EFG:

$$S^{(\mathrm{L})}_{1,M-N} = \sum_{P=-1}^{1} D^{1*}_{M-N,P}(\Omega_{\mathrm{LF}}) S^{(\mathrm{F})}_{1,P} \tag{A6}$$

$$D^{2}_{M0}(\Omega_{\mathrm{LD}}) = \sum_{Q=-2}^{2} D^{2}_{MQ}(\Omega_{\mathrm{LF}}) D^{2}_{Q0}(\Omega_{\mathrm{FD}}) \tag{A7}$$

Combining Eqs. (A4)–(A7) and using a contraction formula for Wigner functions and 3j-symbols [70], we obtain the dipolar Hamiltonian on the desired form

$$H_{IS} = -\bar{\omega}_{\mathrm{D,AN}} \sum_{N=-1}^{1} \sum_{P=-1}^{1} T^{(\mathrm{L})}_{1,N}(I) T^{(\mathrm{F})}_{1,P}(S) E_{NP}(\Omega_{\mathrm{LF}}, \Omega_{\mathrm{FD}}) \tag{A8}$$

with the angular functions

$$E_{NP}(\Omega_{\mathrm{LF}}, \Omega_{\mathrm{FD}}) = \sqrt{30} \sum_{M=-2}^{2} (-1)^{M} \begin{pmatrix} 1 & 2 & 1 \\ P & -M & M-P \end{pmatrix} D^{1}_{N,M-P}(\Omega_{\mathrm{LF}}) D^{2}_{M0}(\Omega_{\mathrm{FD}}) \tag{A9}$$

The dipolar relaxation rate of the amide proton can be obtained from the linear response formula [71]

$$\rho_{\mathrm{AN}}(\omega_0) = \int_0^{\infty} d\tau \frac{\mathrm{Tr}_{IS}\left\{\left[H_I, \tilde{H}_{IS}(\tau)\right][H_{IS}, H_I]\right\}}{\mathrm{Tr}_{IS}\left\{H_I^2\right\}} \tag{A10}$$

where the dipolar Hamiltonian in the first commutator is expressed in the interaction representation

$$\tilde{H}_{IS}(\tau) = e^{i(H_I+H_S)t} H_{IS} e^{-i(H_I+H_S)t} \tag{A11}$$

Combining Eqs. (A8)–(A11), using standard commutation relations [70] and evaluating I-spin traces, we find

$$\rho_{\mathrm{AN}}(\omega_0) = 4\bar{\omega}^{2}_{\mathrm{D,AN}} \mathrm{Re} \sum_{P=-1}^{1} \sum_{P'=-1}^{1} E_{1P}(\Omega_{\mathrm{LF}}, \Omega_{\mathrm{FD}}) E^{*}_{1P'}(\Omega_{\mathrm{LF}}, \Omega_{\mathrm{FD}}) \times \int_0^{\infty} d\tau \exp(i\omega_0\tau) G_{PP'}(\tau) \tag{A12}$$

with the quantum-mechanical S-spin time correlation function

$$G_{PP'}(\tau) = \frac{1}{3}\mathrm{Tr}_S\left\{\exp\left[iH^{(0)}_S\tau\right]\hat{S}^{(\mathrm{F})}_{1,P}(\tau)\exp\left[-iH^{(0)}_S\tau\right]S^{(\mathrm{F})\dagger}_{1,P'}\right\} \tag{A13}$$

where the time-dependent S-spin operators are defined as

$$\hat{S}^{(\mathrm{F})}_{1,P}(\tau) = e^{-iH^{(0)}_S t} e^{iH_S t} S^{(\mathrm{F})}_{1,P} e^{-iH_S t} e^{iH^{(0)}_S t} \tag{A14}$$

The time dependence of $G_{PP'}(\tau)$ reflects coherent evolution under $H^{(0)}_S$ as well as incoherent evolution under $H^{(1)}_S$. To exhibit the former explicitly, we evaluate the S-spin trace in Eq. (A13) in the eigenbasis of the static S-spin Hamiltonian,

$$H^{(0)}_S|k\rangle = E_k|k\rangle \tag{A15}$$

We thus obtain

$$G_{PP'}(\tau) = \frac{1}{3}\sum_k \sum_l \exp\left[-(R^{PP'}_{kl} + i\omega_{kl})\tau\right]\langle k|S^{(\mathrm{F})}_{1,P}|l\rangle\langle k|S^{(\mathrm{F})}_{1,P'}|l\rangle^{*} \tag{A16}$$

where $\omega_{kl} = E_l - E_k$ and $R^{PP'}_{kl}$ are the characteristic decay (or fluctuation) rates of the S-spin system [40,42,43]. Since ^{14}N relaxation is in the extreme motional-narrowing limit (Section 4.1), these rates should not depend on the projection indices P and P'.

Combination of Eqs. (A12) and (A16) now yields

$$\rho_{\mathrm{AN}}(\omega_0) = \frac{2}{9}\bar{\omega}^{2}_{\mathrm{D,AN}} \sum_k \sum_l B_{kl} \frac{R_{kl}}{R^{2}_{kl} + (\omega_0 - \omega_{kl})^{2}} \tag{A17}$$

where

$$B_{kl} = 6\left|\sum_{P=-1}^{1} \langle k|S^{(\mathrm{F})}_{1,P}|l\rangle E_{1P}(\Omega_{\mathrm{LF}}, \Omega_{\mathrm{FD}})\right|^{2} \tag{A18}$$

Among the 9 terms in Eq. (A17) only 3 are 'resonant'. The remaining 6 terms are discarded since they do not contribute significantly to the Q peaks. The Q-peak frequencies correspond to the following S-spin transitions

$$\Omega_{\pm} = E_{\pm1} - E_0 \tag{A19a}$$

$$\Omega_0 = E_1 - E_{-1} \tag{A19b}$$

The coefficients corresponding to these frequencies are

$$B_{\pm} = 6\left|\sum_{P=-1}^{1} \langle 0|S^{(\mathrm{F})}_{1,P}|\pm1\rangle E_{1P}(\Omega_{\mathrm{LF}}, \Omega_{\mathrm{FD}})\right|^{2} \tag{A20a}$$

$$B_0 = 6\left|\sum_{P=-1}^{1} \langle -1|S^{(\mathrm{F})}_{1,P}|1\rangle E_{1P}(\Omega_{\mathrm{LF}}, \Omega_{\mathrm{FD}})\right|^{2} \tag{A20b}$$

Finally, we assume that the relaxation rates R_{kl} are related to the quadrupolar relaxation rate R_{Q} in Eq. (7) as

$$R^{\pm}_{\mathrm{Q}} \equiv R_{0,\pm1} = R_{\mathrm{Q}} \tag{A21a}$$

$$R^{0}_{\mathrm{Q}} \equiv R_{-1,1} = \mu R_{\mathrm{Q}} \tag{A21b}$$

with the constant μ regarded as a model parameter. We thus arrive at Eqs. (29) and (30) of the main text.

To calculate the Q-peak frequencies Ω_α and the associated coefficients B_α, we need the eigenvalues and eigenvectors of $H^{(0)}_S$. Although an analytical solution is available [72], we used a numerical diagonalization of the matrix representation of $H^{(0)}_S$ in the basis of S-spin angular momentum eigenvectors (in the F frame):

$$\mathbf{H}^{(0)}_{\mathrm{S}} = \begin{bmatrix} -\omega_{\mathrm{S}}\cos\beta_{\mathrm{LF}} + \frac{\bar{\omega}_{\mathrm{Q}}}{4} & -\frac{\omega_{\mathrm{S}}}{\sqrt{2}}\sin\beta_{\mathrm{LF}}e^{-i\gamma_{\mathrm{LF}}} & \frac{\eta\bar{\omega}_{\mathrm{Q}}}{4} \\ -\frac{\omega_{\mathrm{S}}}{\sqrt{2}}\sin\beta_{\mathrm{LF}}e^{i\gamma_{\mathrm{LF}}} & -\frac{\bar{\omega}_{\mathrm{Q}}}{2} & -\frac{\omega_{\mathrm{S}}}{\sqrt{2}}\sin\beta_{\mathrm{LF}}e^{-i\gamma_{\mathrm{LF}}} \\ \frac{\eta\bar{\omega}_{\mathrm{Q}}}{4} & -\frac{\omega_{\mathrm{S}}}{\sqrt{2}}\sin\beta_{\mathrm{LF}}e^{i\gamma_{\mathrm{LF}}} & \omega_{\mathrm{S}}\cos\beta_{\mathrm{LF}} + \frac{\bar{\omega}_{\mathrm{Q}}}{4} \end{bmatrix} \tag{A22}$$

Let $\mathbf{V}$ be the eigenvector matrix and $\boldsymbol{\Omega}$ the diagonal eigenvalue matrix. Then

$$\mathbf{H}^{(0)}_S\mathbf{V} = \mathbf{V}\boldsymbol{\Omega} \tag{A23}$$

and

$$\langle k|S^{(\mathrm{F})}_{1,P}|l\rangle = \left(\mathbf{V}^{\dagger}\mathbf{S}_P\mathbf{V}\right)_{kl} \tag{A24}$$

where $\mathbf{S}_P$ is the matrix representation of $S^{(\mathrm{F})}_{1,P}$. In the low-field regime, where

$$\omega_S < \frac{\eta\bar{\omega}_{\mathrm{Q}}}{2} \tag{A25}$$

a perturbation treatment yields the Q-peak frequencies in Eqs. (3)–(5) and the coefficients

$$B_{\pm} = 3|c_{\pm}E_{1,-1}(\Omega_{LF},\Omega_{FD}) \mp c_{\mp}E_{1,1}(\Omega_{LF},\Omega_{FD})|^2 \quad \text{(A26a)}$$

$$B_0 = 12|c_{+}c_{-}E_{1,0}(\Omega_{LF},\Omega_{FD})|^2 \quad \text{(A26b)}$$

where

$$c_{\pm} = \left[\frac{1}{2}\left(1 \pm \frac{\omega_S}{\Delta}\cos\beta_{LF}\right)\right]^{1/2} \quad \text{(A27)}$$

with Δ given by Eq. (5).

The relaxation rate ρ_{AN} depends on the orientation Ω_{LF} mainly via the frequencies Ω_α, which in the low-field regime only depend on β_{LF}. In addition, a dependence on Ω_{LF} enters via the coefficients B_α and the rates R_Q^α. The latter is neglected here. As an approximation, we may also remove the orientation dependence from the coefficients by pre-averaging them over the powder distribution. This leads to the simple expressions in Eq. (33).

The second approach [9] starts from the BWR master equation for the *IS* spin density operator [1] and the spin Hamiltonian in Eq. (A1), but with $H_S = H_S^{(0)}$, that is, *S*-spin fluctuations are not treated explicitly. We first consider the related but different problem of *I*-spin relaxation induced by isotropic modulation of the Euler angles Ω_{LD} in the *I*–*S* dipole coupling in Eq. (A4). The relevant time correlation functions are then

$$\langle D_{NP}^{K}(\Omega_{LD}(\tau))D_{N'P'}^{K'*}(\Omega_{LD}(0))\rangle = \delta_{KK'}\delta_{NN'}\delta_{PP'}\frac{\exp(-\tau/\tau_D)}{(2K+1)} \quad \text{(A28)}$$

The dipolar correlation time, τ_D, may, for example, be the *I*-spin residence time (EMOR mechanism). As in the first approach, this treatment yields an expression for ρ_{AN} as a linear combination of spectral densities at frequencies $\omega_0 - \omega_{kl}$, where we only retain the three 'resonant' terms. Introducing the low-field approximation and pre-averaging the coefficients in the spectral densities, we obtain the same result as from the first approach with these two approximations with the only difference that R_Q^α is replaced by $1/\tau_D$. If the rate of *S*-spin transitions is isotropic (as in the extreme narrowing limit) and level-independent ($R_Q^{\pm} = R_Q^0$), it has the same effect on the *I*-spin relaxation as an orientational randomization of the strong-collision type (A28).

In the third approach, we start from an extended polarization transfer scheme which now includes the ^{14}N spin explicitly (Fig. 14). Note that the spins associated with the amide proton (A) and nitrogen (N) are denoted by *I* and *S*, respectively, in Appendix A. The extended scheme is described by four coupled rate equations, in place of the three in Eq. (11). Evaluating the integral relaxation R_1 defined in Eq. (12), we find that the QP rate R_1^Q, defined in Eq. (15), can still be expressed as the product of a peak rate $\hat{R}$ and a shape function *L*, as in Eq. (16). The expression for $\hat{R}$ is the same as before, Eq. (17), but the shape function in Eq. (18) is replaced by

$$L = \frac{\rho_{AN}}{\rho_{AN}(1 + \kappa R_{IA}/R_Q) + R_{IA}} \quad \text{(A29)}$$

When ^{14}N relaxation is sufficiently fast, meaning $R_Q >> \kappa R_{IA}$, this expression reduces to Eq. (18).

In the simpler scheme of Fig. 8, ρ_{AN} describes relaxation of the amide proton, that is transfer of polarization energy to the lattice. The ^{14}N spin does not appear explicitly, but is treated as a part of the lattice. In the extended scheme of Fig. 14, ρ_{AN} describes coherent and reversible polarization transfer from A to N (that is, from *I* to *S*), with $\kappa = (3/8)\,[\gamma(^1\text{H})/\gamma(^{14}\text{N})]^2 = 71.77$ to satisfy detailed balance. Energy transfer to the lattice occurs in the subsequent step of ^{14}N quadrupolar relaxation. If this step is sufficiently fast, the flow of polarization energy from A to the lattice via N becomes effectively irreversible, as in the simple scheme, and a spin-temperature approach [3,5,73] can be adopted wherein the coherent polarization transfer ρ_{AN} is given by an expression that is formally identical to Eq. (A10) except that $H_S = H_S^{(0)}$ in the spin Hamiltonian of Eq. (1) (as in the second approach).

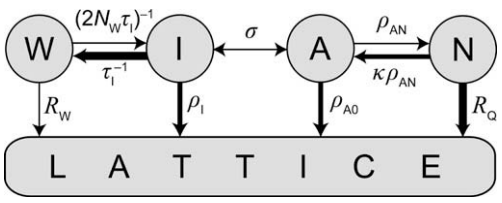

Fig. 14. Extended polarization transfer scheme.

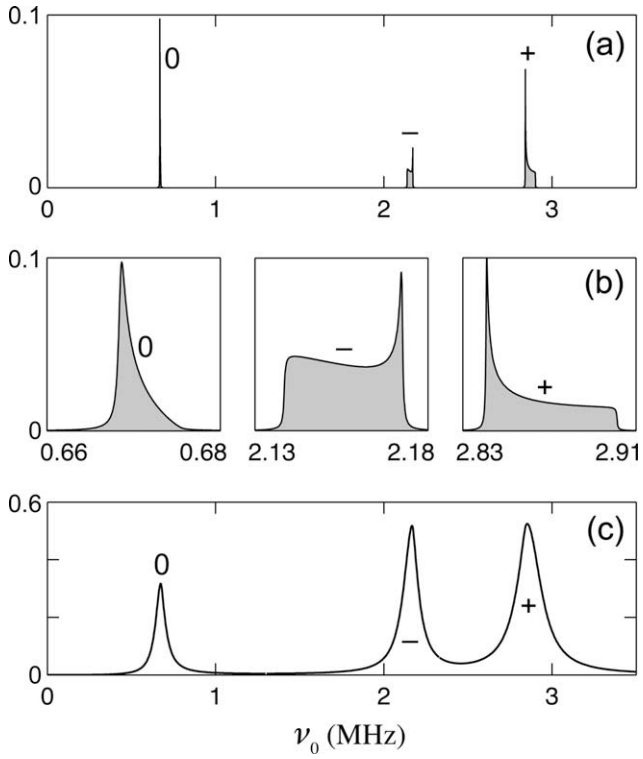

Fig. 15. (a) Frequency dependence of powder-averaged polarization transfer rate, $\langle\rho_{AN}(\omega_0)\rangle$, in units of μs^{-1}. Parameter values: $\nu_Q = 3.34$ MHz, $\eta = 0.4$, $\alpha_{FD} = 0°$, $\beta_{FD} = 90°$, and $R_Q = 2000\ s^{-1}$. (b) Peaks in $\langle\rho_{AN}(\omega_0)\rangle$ on an expanded frequency scale. For $\langle\rho_{AN}^{-}(\omega_0)\rangle$ and $\langle\rho_{AN}^{+}(\omega_0)\rangle$, the amplitude has also been magnified by a factor 4.0 or 1.5, respectively. (c) Frequency dependence of the powder-averaged 'shape factor' $\langle L(\omega_0)\rangle$ for $R_{IA}(2\text{ MHz}) = 25\ s^{-1}$.

The derivation of ρ_{AN} therefore follows the same steps as in the first approach except that $G_{PP'}(\tau)$ in Eq. (A16) now describes purely coherent evolution ($R_{kl}^{PP'} = 0$). The final result for ρ_{AN} is again given by Eq. (A17), but with the Lorentzians replaced by delta functions $\delta(\omega_0 - \omega_{kl})$. However, the Lorentzian form may be reintroduced as an *ad hoc* modification to account for homogeneous broadening of the ^{14}N levels. The only difference between the first and third approach is then the term $\kappa R_{IA}/R_Q$ in Eq. (A29). When this term is <<1, the two approaches are entirely equivalent. For the parameter values required to fit the QP data (Section 5.4), this is not quite the case. For example, in the low-field approximation, the Q_+ peak amplitude of the shape function, $L_+(\Omega_+)$, is ~25% lower in the third approach than in the more rigorous first approach (Fig. 11b).

To illustrate the effect of powder averaging, we show in Fig. 15 the averaged polarization rate $\langle\rho_{AN}(\omega_0)\rangle$ computed with R_Q set to a small value of 2000 s^{-1} to make the homogeneous broadening negligible compared to the inhomogeneous broadening due to the orientation dependence of the frequencies Ω_α. The widths of the peaks in $\langle\rho_{AN}(\omega_0)\rangle$ are only 7 kHz ($\alpha = 0$), 35 kHz (−) and 60 kHz (+), an order-of-magnitude less than the observed Q-peak widths.

Fig. 15 also shows the powder-averaged shape function $\langle L(\omega_0)\rangle$, with $L(\omega_0)$ given by Eq. (A29).

References

[1] A. Abragam, The Principles of Nuclear Magnetism, Clarendon Press, Oxford, 1961.
[2] G. Voigt, R. Kimmich, Quadrupolar dip in the proton relaxation dispersion of poly(vinyl chloride), J. Magn. Reson. 24 (1976) 149–154.
[3] H.T. Stokes, D.C. Ailion, Zeeman-quadrupole cross relaxation between two nuclear spin species, J. Chem. Phys. 70 (1979) 3572–3576.
[4] D. Stephenson, J.A.S. Smith, Nitrogen-14 quadrupole cross-relaxation spectroscopy, Proc. Roy. Soc. Lond. A 416 (1988) 149–178.
[5] L.R. Lichty, J.-W. Han, D.R. Torgeson, R.G. Barnes, E.F.W. Seymour, Cross relaxation between proton and quadrupolar nuclear spins in metal–hydrogen systems, Phys. Rev. B 42 (1990) 7734–7746.
[6] E. Anoardo, D.J. Pusiol, ^{14}N nuclear quadrupole dips in the proton spin–lattice relaxation dispersion in the smectic-*C* phase of HpAB, Phys. Rev. Lett. 76 (1996) 3983–3986.
[7] D. Kruk, O. Lips, Field-dependent nuclear relaxation of spins 1/2 induced by dipole–dipole couplings to quadrupole spins: LaF_3 crystals as an example, J. Magn. Reson. 179 (2006) 250–262.
[8] D. Kruk, F. Fujara, P. Gumann, W. Medycki, A.F. Privalov, C. Tacke, Field cycling methods as a tool for dynamics investigations in solid state systems: recent theoretical progress, Solid State NMR 35 (2009) 152–163.
[9] F. Winter, R. Kimmich, Spin lattice relaxation of dipole nuclei ($I = 1/2$) coupled to quadrupole nuclei ($S = 1$), Mol. Phys. 45 (1982) 33–49.
[10] R. Kimmich, Nuclear magnetic relaxation in the presence of quadrupole nuclei, Z. Naturforsch. 32a (1977) 544–554.
[11] F. Winter, R. Kimmich, NMR field-cycling relaxation spectroscopy of bovine serum albumin, muscle tissue, *Micrococcus luteus* and yeast, Biochim. Biophys. Acta 719 (1982) 292–298.
[12] R. Kimmich, W. Nusser, F. Winter, *In vivo* NMR field-cycling relaxation spectroscopy reveals ^{14}N^{1}H relaxation sinks in the backbones of proteins, Phys. Med. Biol. 29 (1983) 593–596.
[13] R. Kimmich, F. Winter, W. Nusser, K.-H. Spohn, Interactions and fluctuations deduced from proton field-cycling relaxation spectroscopy of polypeptides, DNA, muscles, and algae, J. Magn. Reson. 68 (1986) 263–282.
[14] F. Winter, R. Kimmich, ^{14}N^{1}H and ^{2}H^{1}H cross-relaxation in hydrated proteins, Biophys. J. 48 (1985) 331–335.
[15] S.H. Koenig, Theory of relaxation of mobile water protons induced by protein NH moieties, with application to rat heart muscle and calf lens homogenates, Biophys. J. 53 (1988) 91–96.
[16] S. Peto, P. Gillis, V.P. Henri, Structure and dynamics of water in tendon from NMR relaxation measurements, Biophys. J. 57 (1990) 71–84.
[17] C.C. Lester, R.G. Bryant, Water-proton nuclear magnetic relaxation in heterogeneous systems: hydrated lysozyme results, Magn. Reson. Med. 22 (1991) 143–153.
[18] X. Jiao, R.G. Bryant, Noninvasive measurement of protein concentration, Magn. Reson. Med. 35 (1996) 159–161.
[19] E. Persson, B. Halle, Cell water dynamics on multiple time scales, Proc. Natl. Acad. Sci. USA 105 (2008) 6266–6271.
[20] S.E. Ungersma, N.I. Matter, J.W. Hardy, R.D. Venook, A. Macovski, S.M. Connolly, G.C. Scott, Magnetic resonance imaging with T_1 dispersion contrast, Magn. Reson. Med. 55 (2006) 1362–1371.
[21] P.-O. Westlund, H. Wennerström, Spin–lattice relaxation of a spin-1/2 nucleus coupled to a quadrupolar spin-1 nucleus. The quadrupolar dip, J. Magn. Reson. 63 (1985) 280–286.
[22] D. Kruk, Theory of Evolution and Relaxation of Multi-spin Systems, Arima Publishing, Bury St. Edmunds, Suffolk, UK, 2007.
[23] P.-O. Westlund, Quadrupole-enhanced proton spin relaxation for a slow reorienting spin pair: (*I*)–(*S*). A stochastic Liouville approach, Mol. Phys. 107 (2009) 2141–2148.
[24] S.R. Rabbani, D.T. Edmonds, P. Gosling, M.H. Palmer, Measurement of the ^{14}N quadrupole coupling constants in glycine, diglycine, triglycine, and tetraglycine and a comparison with calculation, J. Magn. Reson. 72 (1987) 230–237.
[25] T. Giavani, H. Bildsøe, J. Skibsted, H.J. Jakobsen, A solid-state ^{14}N magic-angle spinning NMR study of some amino acids, J. Magn. Reson. 166 (2004) 262–272.
[26] I. Migneault, C. Dartiguenave, M.J. Bertrand, K.C. Waldron, Glutaraldehyde: behavior in aqueous solution, reaction with proteins, and application to enzyme crosslinking, Biotechniques 37 (2004) 790–802.
[27] Y. Wine, N. Cohen-Hadar, A. Freeman, F. Frolow, Elucidation of the mechanism and end products of glutaraldehyde crosslinking reaction by X-ray structure analysis, Biotechnol. Bioeng. 98 (2007) 711–718.
[28] A. Wlodawer, J. Walter, R. Huber, L. Sjölin, Structure of bovine pancreatic trypsin inhibitor. Results of joint neutron and X-ray refinement of crystal form II, J. Mol. Biol. 180 (1984) 301–329.
[29] S. Vijay-Kumar, C.E. Bugg, W.J. Cook, Structure of ubiquitin refined at 1.8 Å resolution, J. Mol. Biol. 194 (1987) 531–544.
[30] G. Wagner, Characterization of the distribution of internal motions in the basic pancreatic trypsin inhibitor using a large number of internal NMR probes, Quart. Rev. Biophys. 16 (1983) 1–57.
[31] E. Tüchsen, C. Woodward, Hydrogen kinetics of peptide amide protons at the bovine pancreatic trypsin inhibitor protein–solvent interface, J. Mol. Biol. 185 (1985) 405–419.
[32] E. Tüchsen, J.M. Hayes, S. Ramaprasad, V. Copie, C. Woodward, Solvent exchange of buried water and hydrogen exchange of peptide NH groups hydrogen bonded to buried waters in bovine pancreatic trypsin inhibitor, Biochemistry 26 (1987) 5163–5172.
[33] E. Liepinsh, G. Otting, K. Wüthrich, NMR spectroscopy of hydroxyl protons in aqueous solutions of peptides and proteins, J. Biomol. NMR 2 (1992) 447–465.
[34] D.M. LeMaster, J.S. Anderson, G. Hernández, Peptide conformer acidity analysis of protein flexibility monitored by hydrogen exchange, Biochemistry 48 (2009) 9256–9265.
[35] V.P. Denisov, B. Halle, Protein hydration dynamics in aqueous solution: a comparison of bovine pancreatic trypsin inhibitor and ubiquitin by oxygen-17 spin relaxation dispersion, J. Mol. Biol. 245 (1995) 682–697.
[36] V.P. Denisov, J. Peters, H.D. Hörlein, B. Halle, Using buried water molecules to explore the energy landscape of proteins, Nat. Struct. Biol. 3 (1996) 505–509.
[37] E. Persson, B. Halle, Nanosecond to microsecond protein dynamics probed by magnetic relaxation dispersion of buried water molecules, J. Am. Chem. Soc. 130 (2008) 1774–1787.
[38] C. Mattea, J. Qvist, B. Halle, Dynamics at the protein–water interface from ^{17}O spin relaxation in deeply supercooled solutions, Biophys. J. 95 (2008) 2951–2963.
[39] U. Lindner, Protonenrelaxation in paramagnetischen Lösungen unter Berücksichtigung der Nullfeldaufspaltung, Ann. Physik (Leipzig) 16 (1965) 319–335.
[40] R. Sharp, S.M. Abernathy, L.L. Lohr, Paramagnetically induced nuclear magnetic resonance relaxation in solutions containing $S \geqslant 1$ ions: a molecular-frame theoretical and physical model, J. Chem. Phys. 107 (1997) 7620–7629.
[41] P.-O. Westlund, A low-field paramagnetic nuclear spin relaxation theory, J. Chem. Phys. 108 (1998) 4945–4953.
[42] R. Sharp, L. Lohr, Thermal relaxation of electron spin motion in a thermal equilibrium ensemble: relation to paramagnetic nuclear magnetic resonance relaxation, J. Chem. Phys. 115 (2001) 5005–5014.
[43] R. Sharp, L. Lohr, J. Miller, Paramagnetic NMR relaxation enhancement: recent advances in theory, Progr. NMR Spectrosc. 38 (2001) 115–158.
[44] D. Kruk, T. Nilsson, J. Kowalewski, Nuclear spin relaxation in paramagnetic systems with zero-field splitting and arbitrary electron spin, Phys. Chem. Chem. Phys. 3 (2001) 4907–4917.
[45] J. Kowalewski, D. Kruk, G. Parigi, NMR relaxation in solution of paramagnetic complexes: recent theoretical progress for $S \geqslant 1$, Adv. Inorg. Chem. 57 (2005) 41–104.
[46] E.P. Sunde, B. Halle, Slow internal protein dynamics from water ^{1}H magnetic relaxation dispersion, J. Am. Chem. Soc. 131 (2009) 18214–18215.
[47] A.H. Korn, S.H. Feairheller, E.M. Filachione, Glutaraldehyde—nature of the reagent, J. Mol. Biol. 65 (1972) 525–529.
[48] F. Vaca-Chávez, E. Hellstrand, B. Halle, Hydrogen exchange and hydration dynamics in gelatin gels, J. Phys. Chem. B 110 (2006) 21551–21559.
[49] W.H. Press, S.A. Teukolsky, W.T. Vetterling, B.P. Flannery, Numerical Recipes in C, Cambridge University Press, Cambridge, 1992.
[50] M. Edén, Computer simulations in solid-state NMR. III. Powder averaging, Concepts Magn. Reson. 18A (2003) 24–55.
[51] K.B. Schowen, R.L. Schowen, Solvent isotope effects on enzyme systems, Methods Enzymol. 87 (1982) 551–606.
[52] S.N. Loh, J.L. Markley, Hydrogen bonding in proteins as studied by amide hydrogen D/H fractionation factors: application to *Staphylococcal* nuclease, Biochemistry 33 (1994) 1029–1036.
[53] A.S. Edison, F. Weinhold, J.L. Markley, Theoretical studies of protium/deuterium fractionation factors and cooperative hydrogen bonding in peptides, J. Am. Chem. Soc. 117 (1995) 9619–9624.
[54] Y.W. Bai, J.S. Milne, L. Mayne, S.W. Englander, Primary structure effects on peptide group hydrogen-exchange, Proteins 17 (1993) 75–86.
[55] W.F. Harrington, N.V. Rao, Collagen structure in solution. 1. Kinetics of the helix regeneration in single-chain gelatins, Biochemistry 9 (1970) 3714–3724.
[56] B. Brodsky, A.V. Persikov, Molecular structure of the collagen triple helix, Adv. Protein Chem. 70 (2005) 301–339.
[57] J. Bella, B. Brodsky, H.M. Berman, Hydration structure of a collagen peptide, Structure 3 (1995) 893–906.
[58] F. Vaca-Chávez, B. Halle, Molecular basis of water proton relaxation in gels and tissue, Magn. Reson. Med. 56 (2006) 73–81.
[59] M. van der Rest, R. Garrone, Collagen family of proteins, FASEB J. 5 (1991) 2814–2823.
[60] R.E. Stark, R.A. Haberkorn, R.G. Griffin, ^{14}N NMR determination of NH bond lengths in solids, J. Chem. Phys. 68 (1978) 1996–1997.
[61] J.G. Hexem, M.H. Frey, S.J. Opella, Molecular and structural information from ^{14}N–^{13}C dipolar couplings manifested in high resolution ^{13}C NMR spectra of solids, J. Chem. Phys. 77 (1982) 3847–3856.
[62] Q. Teng, M. Iqbal, T.A. Cross, Determination of the ^{13}C chemical shift and ^{14}N electric field gradient tensor orientations with respect to the molecular frame in a polypeptide, J. Am. Chem. Soc. 114 (1992) 5312–5321.
[63] M.D. Esrafili, H. Behzadi, N.L. Hadipour, Density functional theory study of N–H…O, O–H…O and C–H…O hydrogen-bonding effects on the ^{14}N and ^{2}H

nuclear quadrupole coupling tensors of *N*-acetyl-valine, Biophys. Chem. 133 (2008) 11–18.
[64] D. Lankhorst, J. Schriever, J.C. Leyte, An NMR relaxation study of hydrogen exchange and its deuterium isotope effects in aqueous carboxylic acid solutions, Chem. Phys. 77 (1983) 319–340.
[65] M. Sundd, N. Iverson, B. Ibarra-Molero, J.M. Sanchez-Ruiz, A.D. Robertson, Electrostatic interactions in ubiquitin: stabilization of carboxylates by lysine amino groups, Biochemistry 41 (2002) 7586–7596.
[66] B. Halle, Molecular theory of field-dependent proton spin–lattice relaxation in tissue, Magn. Reson. Med. 56 (2006) 60–72.
[67] B. Halle, Spin dynamics of exchanging quadrupolar nuclei in locally anisotropic systems, Progr. NMR Spectrosc. 28 (1996) 137–159.
[68] B. Halle, Protein hydration dynamics in solution: a critical survey, Philos. Trans. R. Soc. Lond. B 359 (2004) 1207–1224.
[69] K. Venu, L.A. Svensson, B. Halle, Orientational order and dynamics of hydration water in a single crystal of bovine pancreatic trypsin inhibitor, Biophys. J. 77 (1999) 1074–1085.
[70] D.M. Brink, G.R. Satchler, Angular Momentum, Clarendon, Oxford, 1968.
[71] R. Kubo, K. Tomita, A general theory of magnetic resonance absorption, J. Phys. Soc. Jpn. 9 (1954) 888–919.
[72] G.M. Muha, The Zeeman effect in spin = 1 systems, J. Magn. Reson. 49 (1982) 431–443.
[73] M. Goldman, Spin Temperature and Nuclear Magnetic Resonance in Solids, Clarendon Press, Oxford, 1970.